JOURNAL OF GEOPHYSICAL RESEARCH, VOL. 113, D04213, doi:10.1029/2007JD009095, 2008

Impacts of 3-D radiative effects on satellite cloud detection and their consequences on cloud fraction and aerosol optical depth retrievals

Yuekui Yang[1,2] and Larry Di Girolamo[1]

Received 24 June 2007; revised 17 October 2007; accepted 20 November 2007; published 29 February 2008.

[1] We present the first examination on how 3-D radiative transfer impacts satellite cloud detection that uses a single visible channel threshold. The 3-D radiative transfer through predefined heterogeneous cloud fields embedded in a range of horizontally homogeneous aerosol fields have been carried out to generate synthetic nadir-viewing satellite images at a wavelength of 0.67 μm. The finest spatial resolution of the cloud field is 30 m. We show that 3-D radiative effects cause significant histogram overlap between the radiance distribution of clear and cloudy pixels, the degree to which depends on many factors (resolution, solar zenith angle, surface reflectance, aerosol optical depth (AOD), cloud top variability, etc.). This overlap precludes the existence of a threshold that can correctly separate all clear pixels from cloudy pixels. The region of clear/cloud radiance overlap includes moderately large (up to 5 in our simulations) cloud optical depths. Purpose-driven cloud masks, defined by different thresholds, are applied to the simulated images to examine their impact on retrieving cloud fraction and AOD. Large (up to 100s of %) systematic errors were observed that depended on the type of cloud mask and the factors that influence the clear/cloud radiance overlap, with a strong dependence on solar zenith angle. Different strategies in computing domain-averaged AOD were performed showing that the domain-averaged BRF from all clear pixels produced the smallest AOD biases with the weakest (but still large) dependence on solar zenith angle. The large dependence of the bias on solar zenith angle has serious implications for climate research that uses satellite cloud and aerosol products.

Citation: Yang, Y., and L. Di Girolamo (2008), Impacts of 3-D radiative effects on satellite cloud detection and their consequences on cloud fraction and aerosol optical depth retrievals, *J. Geophys. Res.*, *113*, D04213, doi:10.1029/2007JD009095.

1. Introduction

[2] Cloud detection is a fundamental step in satellite data analysis that directly impacts the quality of many satellite geophysical products used in weather, climate and environmental research [e.g., *Rossow et al.*, 1985; *Wielicki and Parker*, 1992; *Weare*, 1995; *Stowe et al.*, 1999; *Myhre et al.*, 2004; *Kaufman et al.*, 2005]. As a result, continuing efforts are being made toward developing advanced cloud detection algorithms and characterizing their uncertainties [e.g., *Rossow and Garder*, 1993a; *Ackerman et al.*, 1998; *Berendes et al.*, 2004; *Thomas et al.*, 2004; *Zhao and Di Girolamo*, 2006; *Yang et al.*, 2007]. Currently all operational satellite cloud detection algorithms use thresholds to distinguish clear pixels from cloudy ones. These thresholds are applied to an observed quantity, call it an observable, such as the radiance, the bidirectional reflectance factor (BRF), a combination of different spectral channel radiance, etc. [e.g., *Saunders and Kriebel*, 1988; *Ackerman et al.*, 1998; *Baum and Trepte*, 1999; *Stowe et al.*, 1999; *Yang et al.*, 2007]. For example, if the observable value of a pixel is greater than a threshold, then the pixel is ''cloudy''; otherwise it is ''clear''. We use the BRF in the visible portion of the electromagnetic spectrum as our working example throughout this study, where the BRF is defined as:

$$BRF = \frac{\pi L}{\mu_0 F_0}$$

where L is the spectral radiance at the top of the atmosphere, μ_0 is the cosine of the solar zenith angle and F_0 is the solar spectral irradiance at the top of the atmosphere.

[3] Ideally, the threshold method can work perfectly (i.e., no errors) when a discontinuity in the BRF frequency distribution (histogram) exists with all clear pixels on one side of the threshold and all cloudy pixels on the other side. Yet observations over a wide range of space and timescales have shown that the BRF frequency distribution always forms a continuum [e.g., *Wielicki and Welch*, 1986;

[1]Department of Atmospheric Sciences, University of Illinois at Urbana-Champaign, Urbana, Illinois, USA.
[2]Now at Goddard Earth Science and Technology Center, University of Maryland at Baltimore County, Baltimore, Maryland, USA.

0148-0227/08/2007JD009095$09.00

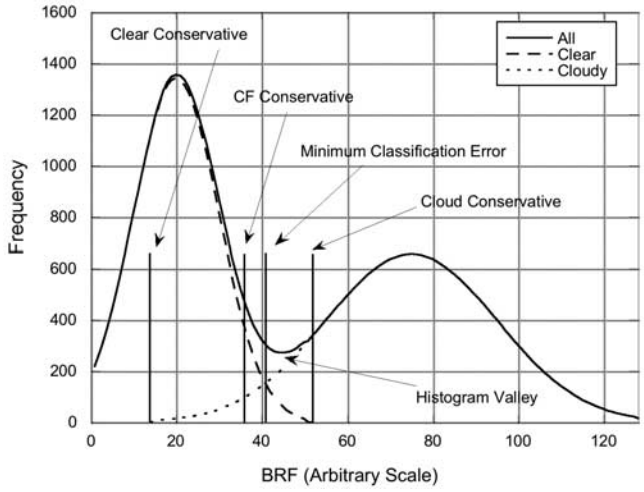

Figure 1. A conceptual model of a BRF histogram of a satellite image. The distributions of clear and cloudy pixels are assumed to be Gaussian. The three histograms are for clear pixels, cloudy pixels, and all pixels. Four types of thresholds are shown in the figure: the minimum classification error (MCE) threshold, the cloud fraction (CF) conservative threshold, the clear conservative threshold, and the cloud conservative threshold.

Rossow, 1989; *Wielicki and Parker*, 1992; *Rossow and Garder*, 1993b; *Koren and Joseph*, 2000; *Yang et al.*, 2007]. To help elucidate cloud detection issues that arise from a continuous histogram, Figure 1 shows a histogram for a fictitious image, composed of 256 × 256 pixels in size and having a cloud fraction of 50%. The histogram was generated by assuming both the distributions of clear and cloudy pixels to be Gaussian. The clear pixel distribution has a mean of 20 and a standard deviation of 10; the cloudy pixel distribution has a mean of 75 and a standard deviation of 20. Note for this continuous histogram, the distributions of clear pixels and cloudy pixels are overlapped. The overlapped region is the area under both clear and cloudy distributions. With overlap, perfect cloud detection through thresholding becomes impossible because no single threshold could separate all clear pixels from cloudy pixels. Where to place the threshold will depend on the purpose of cloud detection. For example, since we know the distributions of clear and cloudy pixel BRFs in Figure 1, four different thresholds are calculated for this histogram and shown in the figure: the minimum classification error (MCE) threshold, which minimizes misclassification; the cloud fraction (CF) conservative threshold, which gives the correct cloud fraction; the clear conservative threshold, which gives no misclassified cloudy pixels; and the cloud conservative threshold, which gives no misclassified clear pixels. No single threshold would suit all purposes. For example, a clear conservative threshold may be desirable for clear sky analysis (e.g., for retrieving surface properties), while a cloud conservative threshold may be desirable for the retrieval of cloud properties. A good threshold is one that serves its purpose.

[4] In practice, since neither the clear pixel distribution nor the cloudy pixel distribution is known, a variety of algorithms have been developed to derive the suitable threshold [e.g., *Rossow et al.*, 1985; *Yang et al.*, 2007]. A large portion of these algorithms are pursuing the MCE threshold [e.g., *Strahler*, 1980; *Kittler and Illingworth*, 1986; *Pal and Bhandari*, 1993]. Note that even though the valley of a histogram has been used as a substitute of the MCE threshold [e.g., *Prewitt and Mendelsohn*, 1966; *Glasbey*, 1993], the valley itself is not necessarily the MCE threshold as shown in Figure 1.

[5] Since it is the overlap between clear and cloudy pixel distributions that makes perfect thresholding impossible and leads to a number of potential thresholds to be defined, understanding the causes of it becomes critical to satellite cloud detection research and application. It has been pointed out that background variability and instrument noise are two contributors [e.g., *Wielicki and Parker*, 1992; *Yang et al.*, 2007]. However, there has been no study that examines the impacts of another potentially important factor, the 3-D radiative effects, on the histogram shapes and hence on cloud detection.

[6] Numerous studies have provided significant insights on how 3-D radiative effects impact the radiance/BRF fields [e.g., *Marshak et al.*, 1995; *Loeb and Davies*, 1997; *Di Girolamo et al.*, 1998; *Várnai and Marshak*, 2003; *Nikolaeva et al.*, 2005], the retrieval of cloud properties [e.g., *Loeb and Coakley*, 1998; *Várnai and Marshak*, 2001; *Marshak et al.*, 2006], and the retrieval of aerosol optical depth [e.g, *Cahalan et al.*, 2001; *Wen et al.*, 2001; *Wen et al.*, 2006]. There are many different pathways that 3-D effects can affect the BRF field. Some roughen it and some smooth it [e.g., *Várnai and Marshak*, 2003; *Nikolaeva et al.*, 2005]. However, only those pathways that make the BRF of a clear pixel brighter or a cloudy pixel darker have impacts on satellite cloud detection because they would lower the distinguishability between clear and cloudy pixels. Figure 2 depicts four representative pathways with which 3-D radiative effects contribute to this problem, specifically, on how the BRF of pixel A is affected by 3-D effects. These four pathways are the following:

[7] 1. Clear pixel BRF enhancement through the channeling pathway. Figure 2a shows that the BRF of the clear pixel A is enhanced by the extra scattering of radiation from the cloudy pixel B. Photons scattered back by the cloudy pixel B could reach the sensor through additional scattering by the atmospheric molecules and aerosol particles within clear pixel A. This panel is similar to Figure 2a by *Várnai and Marshak* [2003].

[8] 2. Cloudy pixel BRF reduction through the leakage pathway. In Figure 2b, cloud pixel A is darkened due to radiation leaking into the area of smaller extinction coefficient (clear pixel B).

[9] 3. Cloudy pixel BRF reduction through the shadowing pathway. Figure 2c depicts that cloudy pixel A is darkened because of the shadow cast by a higher cloudy pixel (pixel B).

[10] 4. Clear pixel BRF enhancement through the surface-cloud interaction pathway (Figure 2d). Radiation diffused by clouds can be reflected back by the surface and reach the satellite sensor after passing through the clear pixel A. In this case, the BRF of pixel A is enhanced.

[11] The goal of this study is to further understand how 3-D radiative effects contribute to cloud detection errors through these basic pathways. We also examine how these errors are carried over to the retrieval of cloud fraction and aerosol optical depth for the variety of thresholds depicted in

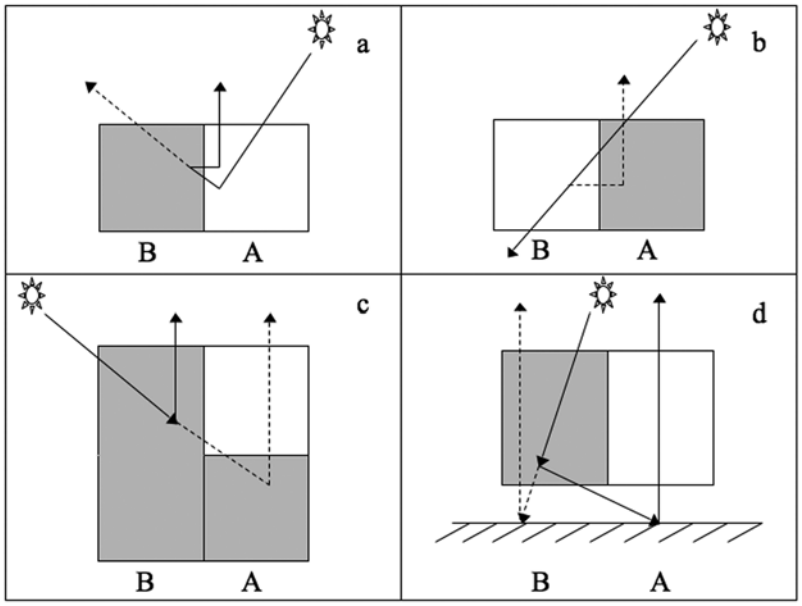

Figure 2. 3-D pathways that may result in histogram overlap by causing a clear pixel to appear brighter (pixel A in Figures 2a and 2d) or a cloudy pixel to appear darker (pixel A in Figures 2b and 2c). The arrows with the solid lines are the photon paths in the 3-D field; the arrows with the dashed lines would be the photon paths if the field was homogenous with the properties of pixel A. Darker color indicates cloudy and white indicates clear. Figure 2a is similar to Figure 2a by *Várnai and Marshak* [2003].

Figure 1. As will be shown in this article, these basic pathways can lead to overlap between clear and cloudy BRF distributions in the absence of surface variability and instrument noise, which causes uncertainties in satellite cloud detection and subsequently affect the retrieval of both cloud and aerosol properties.

[12] To achieve this goal, we adopt the 3-D radiative transfer model SHDOM (Spherical Harmonics Discrete Ordinate Method) [*Evans*, 1998]. The radiative transfer process through predefined heterogeneous cloud fields embedded in a range of aerosol fields are simulated over a Lambertian surface to generate synthetic satellite images at nadir at the wavelength of 0.67 μm. Thresholding with the 0.67 μm BRF is a popular cloud detection test [e.g., *Saunders and Kriebel*, 1988; *Rossow and Garder*, 1993b; *Ackerman et al.*, 1998; *Baum and Trepte*, 1999; *Stowe et al.*, 1999], and by itself detects most of the clouds over ocean in the MODIS operational cloud mask product [*Ackerman et al.*, 2007]. The procedures of cloud detection followed by cloud fraction and aerosol optical depth retrieval are applied to these synthetic images to analyze the impacts of 3-D radiative effects. Details about the simulations are described in section 2. Section 3 discusses the 3-D radiative effects on BRF frequency distributions. Section 4 shows the impacts of 3-D effects on satellite cloud detection and cloud fraction. The consequences on aerosol optical depth retrieval are analyzed in section 5 and finally the results are summarized in section 6.

2. Simulations

[13] Two cloud fields are used in the simulations, each with two different types of vertical structure variability. Figure 3 gives the optical depth distributions of the cloud fields adopted in this study. Figures 3a and 3b show a scale invariant field and the corresponding distribution of the cloud optical depths. The scale invariant field is created with the fractal model described by *Várnai* [1996] with a scaling exponent of 3.0. The image size is 256 by 256 pixels with a spatial resolution of 30 m and 17 vertical layers. The cloud fraction is 60% and the mean cloud optical depth is 4. To study the effect of cloud top inhomogeneity, two different 3-D cloud fields are generated based on this optical depth field, one by assuming that the optical depth distribution is caused by cloud top height variability with a constant extinction coefficient (bumpy cloud top case), the other by assuming that the optical depth distribution is caused by extinction coefficient horizontal variability with a constant cloud top height of 900 m (flat cloud top case). The cloud base altitude for both cases is 600 m.

[14] Figures 3c and 3d are a cumulus field and the corresponding distribution of the cloud optical depths. This field is generated by a Large Eddy Simulation (LES). It is one of the fields used by the International Intercomparison of 3-D Radiation Codes (I3RC) Phase 2 [*Cahalan et al.*, 2005]. The size of the scene is 100 by 100 grid points with a resolution of 67 m with 42 vertical layers. The cloud fraction is 29% and the mean cloud optical depth is 22. A flat top case is also generated by adopting a constant cloud top height of 2.3 km. The cloud base of this case varies from 1.02 km to 2.30 km with an average of 1.27 km.

[15] While the properties of these two cloud fields fall within the distribution of cumulus cloud properties observed in nature, they were simply chosen to give moderately low and moderately high cloud fraction and optical depth scenes. It is certain that these cloud fields do not represent the complete range of cloud variability observed in nature, but they should serve as a good starting point in providing

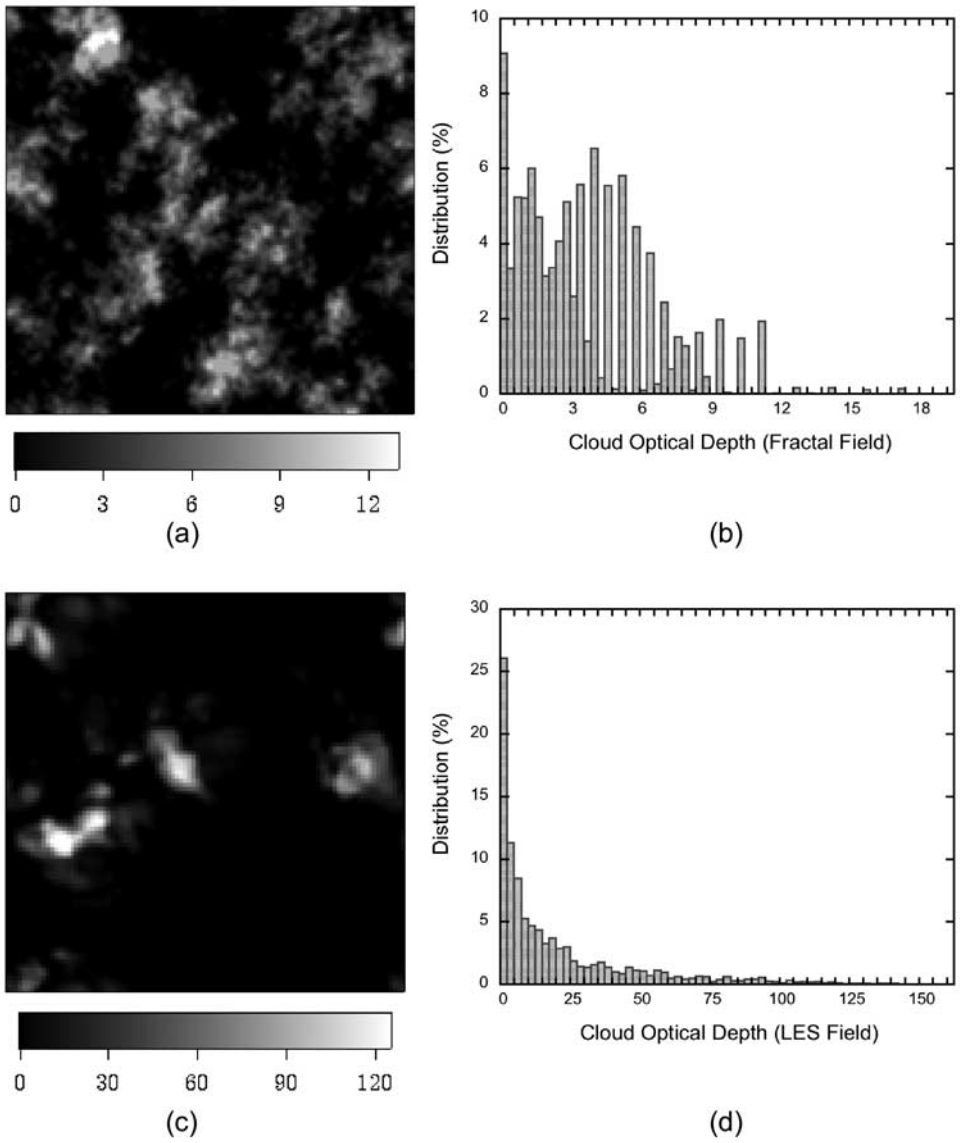

Figure 3. The cloud optical depth fields used in this study. (a) The fractal cloud field, (b) the distribution of the cloud optical depths of Figure 3a, (c) Large Eddy Simulation cloud field, and (d) the distribution of the cloud optical depths of Figure 3c.

insight into how 3-D radiative transfer affects satellite cloud detection and aerosol retrievals.

[16] For simplicity, aerosols are monoradius with a value of 1 μm with a real and imaginary part of the refractive index of 1.55 and 0.01, respectively. The aerosol mass concentration is horizontally homogeneous and distributed vertically based on the scaling profile shown in Figure 4. The scale factor is multiplied by a constant to give the vertical profile of aerosol mass concentration and this constant is adjusted to give a variety of aerosol optical depths used in the simulations. The scaling factor employed here is similar to what is used in the MODTRAN maritime aerosol model [*Acharya et al.*, 1998].

[17] The simulations are carried out at the wavelength of 0.67 μm. Factors such as molecular scattering, aerosol optical depth, surface reflectance, solar zenith angle, and horizontal spatial resolution are examined in terms of their impact on the BRF distributions. When present, the surface is assumed to be Lambertian with 5% reflectance. In SHDOM, the radiative transfer source function is computed on a discrete spatial grid with the angular distribution represented in a spherical harmonic series. Details about the model are given by *Evans* [1998]. Because SHDOM defines cloud fields on grid points, four grid points enclose a pixel on the horizontal plane. In our analysis, if one of the four grid points is cloudy, then we regard the whole pixel as completely cloudy. This is physically consistent with how radiative transfer is calculated in the SHDOM model, which assumes that the variation in the extinction across a grid cell is linear.

[18] Because of limited computational power, only the scenes discussed in Figure 3 are used in SHDOM, and the domain sizes of these scenes are rather small when considering the radiative interaction scales between neighboring clear and cloudy pixels [e.g., *Wen et al.*, 2001]. Hence by no means are the errors in cloud detection, cloud fraction and aerosol optical depth retrieval shown in this study represen-

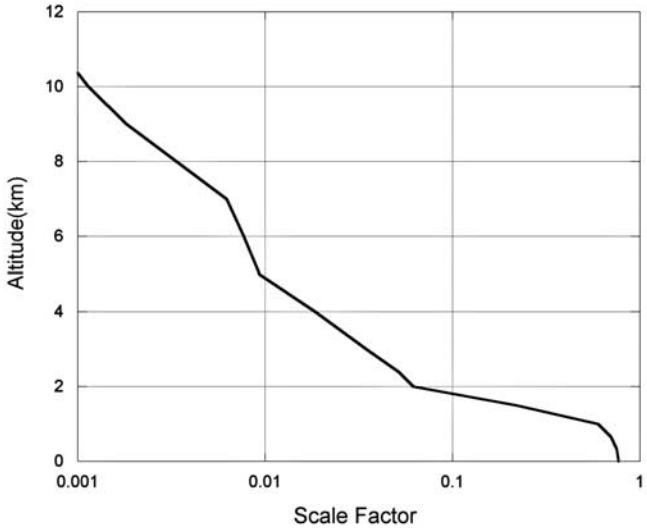

Figure 4. The scale factor for vertical aerosol distribution used in this study.

tative of the quality of any operational products. Rather, we seek physical insight on the connection between these three retrievals caused by 3-D radiative transfer.

3. Controls on the BRF Histogram

3.1. BRF Histogram from the Independent Pixel Approximation

[19] It is instructive to first run simulations with SHDOM under the independent pixel approximation (IPA), which applies 1-D radiative transfer to individual model columns. This will act as a basis for comparison for full 3-D radiative transfer simulations. Figure 5 shows the histogram distribution of the simulated BRF image for the fractal case with bumpy top for overhead sun. Under this situation, all the cloudy pixels are brighter than the clear pixels. The clear pixels have the same BRF value of 0.08. Since there is no overlap between the distributions of clear and cloudy pixels, perfect cloud detection is achievable through thresholding for the IPA case. For example, if we choose 0.09 as the threshold, there will be no misclassification because all the cloudy pixels have a BRF > 0.09 and all the clear pixels have a BRF < 0.09. For oblique sun and other cloud field simulations, the conclusions are the same: a threshold exists that separates all clear pixels from the cloudy pixels because under IPA, all the clear pixels have the same BRF value that is lower than the BRF values of all cloudy pixels.

3.2. Impact of Molecular, Aerosol and Surface Scattering on BRF Histogram

[20] Figure 6 gives the evolution of BRF histograms as molecular scattering, aerosol scattering, and surface reflectance are added to the model under full 3-D radiative transfer simulations for the fractal field with bumpy top case. Figures 6a to 6f are for overhead Sun and Figures 6a' to 6f' are for $\mu_0 = 0.5$. For overhead Sun, the shadowing pathway (Figure 2c) does not exist. Figure 6a shows the distributions of clear and cloudy pixels when no atmosphere and no surface are present. Since no clear-pixel BRF enhancements through channeling (Figure 2a) and surface-cloud interaction (Figure 2d) pathways can take place under this situation, all clear pixels have a BRF value of 0. If molecular scattering is added (Figure 6b), the channeling pathway arises and adds variance to the clear-pixel BRFs. With the addition of aerosol (Figure 6c), the channeling pathway increases and the mean and variance of the clear-pixel BRFs increases as well compared to Figure 6b. As the surface reflection (Figure 6d) is taken into account, the mean BRF increases (as would be expected even without any 3-D radiative interaction) and the surface-cloud interaction pathway occurs and results in a much larger clear-pixel BRF variance.

[21] In company with the change of the clear pixel distributions, cloudy pixel distributions change as well. As molecular scattering, aerosol scattering, and surface reflectance are added to the model, the BRF values of cloudy pixels increase and the difference between the darkest cloudy pixels and the brightest clear pixels decreases. This is due to the fact that while some of the clear pixels are brightened through the channeling and surface-cloud interaction pathways, their neighboring cloudy pixels can be darkened compared to IPA simulations through the leakage pathway. Figure 6d and Figure 5 share the same atmosphere, cloud and surface conditions, where the differences in the results arise from 3-D radiative effects. When 3-D radiative effects are taken into account (Figure 6d), the clear-pixel BRFs have a non-zero variance. As atmosphere and surface conditions change, the BRF variance caused by 3-D radiative effects can result in overlap between clear and cloudy pixel distributions. As shown in Figures 6e and 6f, overlap between clear and cloud distributions takes place at large AOD values under these particular simulations.

[22] At $\mu_0 = 0.5$, the shadowing pathway plays an important role. When there is no atmosphere and no surface (Figure 6a'), all the clear pixels still have the same BRF value of 0 because no pathways exist that could lead to clear-pixel BRF enhancement or reduction. However, the shadowing and leakage pathways cause some cloudy pixels to become

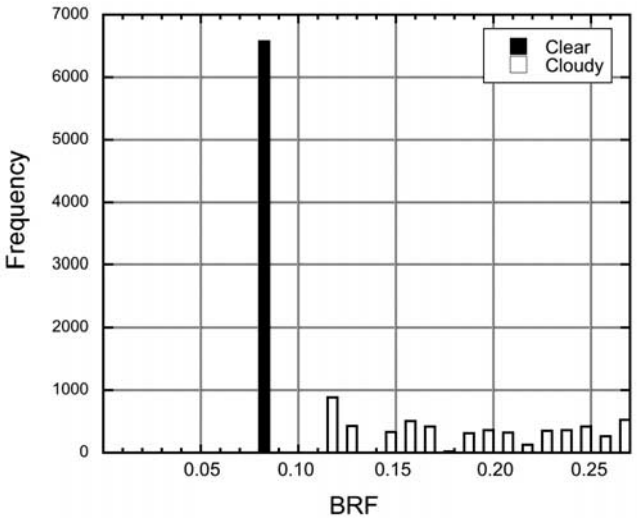

Figure 5. The 128-bin histogram of the fractal cloud field with bumpy cloud top calculated under independent pixel approximation for overhead Sun. Molecular scattering is included, aerosol optical depth is 0.1, and the surface is Lambertian with a reflectance of 5%.

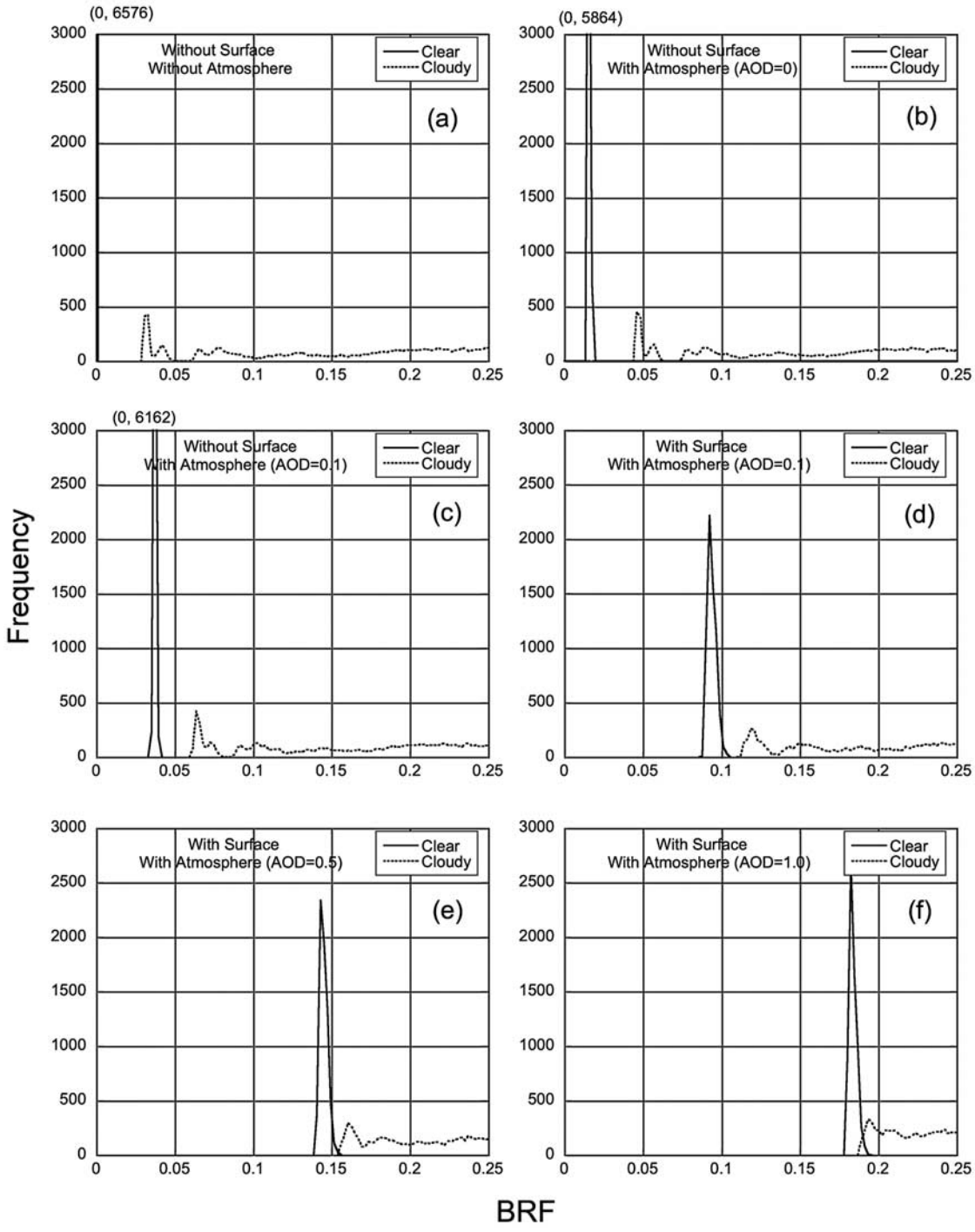

Figure 6. BRF histograms of clear and cloudy pixels for the fractal cloud field with bumpy cloud top. Figures 6a, 6b, 6c, 6d, 6e, and 6f are for simulations under overhead Sun, and Figures 6a', 6b', 6c', 6d', 6e', and 6f' are results for $\mu_0 = 0.5$. When present, the surface is Lambertian with a reflectance of 5%. The effect of different aerosol optical depth (AOD) is also shown. The data pairs on top of Figures 6a, 6b, 6c, 6a', 6b', and 6c' are the location and frequency values of the corresponding peaks of the clear pixel distribution. The bin width of the histograms is 0.002.

darker than the overhead Sun case, but all the cloudy pixel BRFs remain brighter than the clear pixels; hence perfect cloud detection through thresholding is still possible in this case. When molecular scattering is considered, the channeling, leakage and shadowing pathways all take place, which results in some of the clear pixels being brighter than some cloudy pixels; hence, overlap between clear and cloud distributions occurs (Figure 6b'). With the addition of aerosol (Figure 6c'), the overlap region increases. As surface is added to the simulations (Figures 6d', 6e', and 6f'), the surface-cloud interaction pathway takes place and overlap becomes much more prominent.

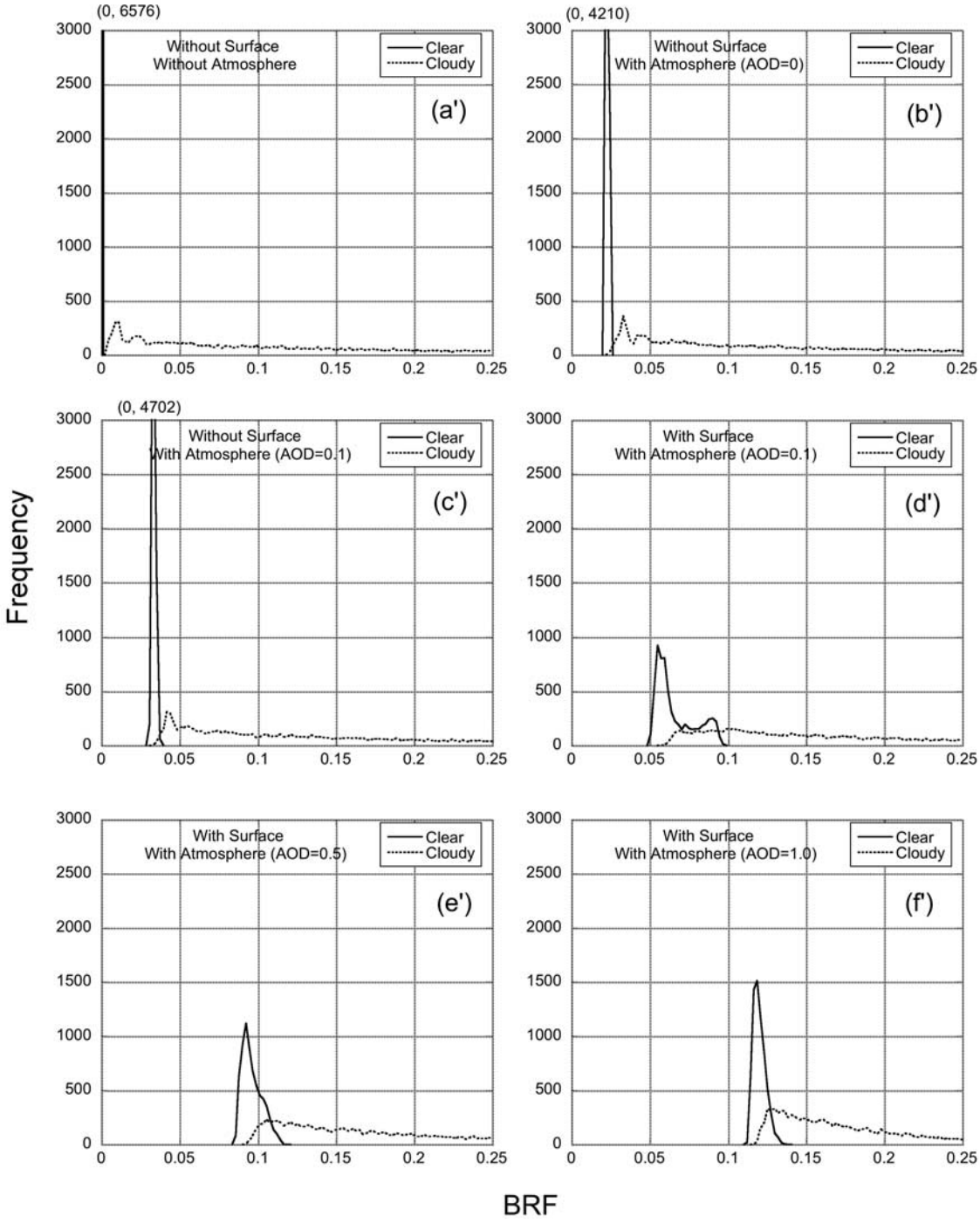

Figure 6. *Continued*. Figures 6a', 6b', 6c', 6d', 6e' and 6f' are the same as Figures 6a, 6b, 6c, 6d, 6e and 6f, except for $\mu_0 = 0.5$.

[23] For the simulations with the LES cloud with bumpy top case (not shown), no overlap occurs between the distributions of clear and cloudy pixels under 1-D assumption or when there is no atmosphere for 3-D simulations (same as the conclusions drawn from the fractal case with bumpy top). Overlap occurs if molecular scattering is added to the simulation for the LES case even for overhead Sun. This is different than the simulations for the fractal field, as shown in Figure 6b, where no overlap exists if only molecular scattering is considered under overhead Sun. The reason for the difference is that the minimum cloud optical depth for the LES case is around 0.005, while it is 0.2 for the fractal case.

[24] The changes (not shown) in histogram shape for the flat top cases for both fields are similar to their bumpy top counterparts. These results show that molecular scattering, aerosol scattering, and surface reflection all contribute to the overlap of the distributions of clear and cloudy pixels, which leads to satellite cloud detection problems as quantified in section 4.

3.3. Pixel Resolution

[25] The spatial resolution of the pixel also controls the shape of the histogram and the degree to which clear, cloudy, and partially cloudy pixels overlap. To study this effect, coarser resolution images are generated by averaging the BRF values of neighboring pixels of the original full resolution simulations. For example, to degrade the resolution by a factor of two, the BRF values of four neighboring pixels are averaged and the mean is used as the BRF of the new coarser resolution pixel. Figure 7 displays how the change of spatial resolution affects histogram shape, threshold, and cloud fraction for the case given in Figure 6d. As shown in Figure 6d, no overlap exists for the simulated full resolution BRF histogram. However, when the image resolution is degraded by a factor of 2 (Figure 7a), an overlap occurs between the distributions of clear pixels and partially cloudy pixels. Analysis of the degraded image reveals that the overlap occurs when some full-resolution cloudy pixels with low BRF values are combined with surrounding full-resolution clear pixels, the newly formed partially cloudy coarse-resolution pixels have a smaller BRF value than some bright clear coarse-resolution pixels.

[26] As the spatial resolution becomes coarser, larger portions of the image pixels contain some (either fully or partially) cloud. Figure 7b illustrates that the fraction of pixels containing some cloud reaches 100% when the image resolution is degraded by a factor of 16 for the case shown. To have a correct cloud fraction, the threshold must increase as the resolution decreases. On the other hand, if the threshold is kept constant, the derived cloud fraction increases as resolution decreases. These simulated results are consistent with the analysis of *Wielicki and Parker* [1992].

3.4. Solar Zenith Angle

[27] Figure 8 shows the dependence of histogram shape on solar zenith angle, for the fractal cloud field with bumpy top case at full resolution. As shown in the figure, there is no overlap between the BRF distributions of clear and cloudy pixels for overhead Sun ($\mu_0 = 1$), and there is overlap for all oblique sun angles ($\mu_0 \leq 0.9$). From the histograms we can see that the overlap for oblique Sun is mainly due to a subset of cloudy pixels that have very small BRF values. For $\mu_0 = 0.9$, the distribution of clear pixels becomes bimodal, with a small peak on the left, which arises from shadowed clear pixels. For more oblique Sun ($\mu_0 < 0.9$), the clear-pixel shadow peak becomes more prominent. At $\mu_0 = 0.3$, almost all clear pixels are shadowed and the clear pixel distribution returns to unimodal.

[28] A natural question is: where are the overlapped pixels located? Figure 9a is the simulated BRF image for the fractal field with bumpy top at the solar zenith angle of $\mu_0 = 0.5$. The image shows visibly that some of the clear pixels are brighter than others. Figure 9b displays the shadowed versus non-shadowed regions calculated based on the geometry of clouds and the position of the Sun. The darker clear pixels in Figure 9a are shadowed by clouds, while brighter ones are not. Figure 9c gives overlapped versus non-overlapped pixels. Comparing Figures 9a, 9b, 9c with the optical depth image (Figure 3a), we can see that overlapped clear pixels tend to occur when they are not shadowed by the cloud, but are near cloud edges, which is a result of the contributions from the channeling and the surface-cloud interaction pathways (Figures 2a and 2d); overlapped cloudy pixels tend to occur when they are shadowed by other clouds, or when they are optically thin, which is a result of the contributions from the leakage and shadowing pathways (Figures 2a and 2c).

4. Impacts of 3-D Radiative Effects on Cloud Detection and Cloud Fraction Retrieval

[29] In the absence of clear and cloud overlap in the BRF histogram, perfect cloud detection is achievable through a single BRF threshold. However, the presence of overlap leads to a variety of ways in which a threshold may be defined, each for different purposes of the cloud mask. Four such thresholds were defined in Figure 1. These four thresholds were applied to our simulations of BRF. As an example, Figure 10 gives the cloud masks for the BRF image shown in Figure 9a and Table 1 gives the corresponding cloud fraction derived from each threshold as well as the percentage of misclassification that comes from misclassified clear/cloudy pixels. Figure 10a is the perfect (i.e., no classification errors) cloud mask based on the input cloud field to the simulations. No threshold for the BRF image exists that can reproduce the perfect cloud mask. As discussed in section 1, the cloud mask from the MCE threshold (Figure 10b) minimizes the total misclassification and most of the misclassification comes from misclassified cloudy pixels (Table 1). As a result of misclassifying an equal amount of clear and cloudy pixels (Table 1), the cloud fraction conservative threshold (Figure 10c) gives the correct cloud fraction, which is defined as the number of cloudy pixels in the perfect cloud mask (Figure 10a) divided by the total number of pixels. As expected, the cloud conservative threshold (Figure 10d), which gives no misclassified clear pixels, underestimates the cloud fraction (by 18%, for this example, Table 1), while the cloud mask derived from the clear conservative threshold (Figure 10e), which gives no misclassified cloudy pixels, highly overestimates the cloud fraction (by 29% for this example, Table 1).

[30] The misclassification rate from the MCE threshold can serve as a cloud detection difficulty index. Figure 11 shows the misclassification rate for the MCE threshold as a function of solar zenith angle. For the cases studied here, the misclassification rate is at a minimum for overhead Sun due to the absence of the shadowing pathway. When the Sun is not overhead, the shadowing pathway takes place and contributes to the overlap between clear and cloudy pixel distributions. However, shadows can also cause some clear pixels to be darker, which reduces histogram overlap. Overlap can also be reduced by other 3-D pathways. For example, compared to being in a uniform cloudy field (1-D), a cloudy pixel can be brightened when adjacent to a clear pixel because of cloud side illumination (For detailed discussion on this topic, see *Várnai and Marshak* [2003]). Because the misclassification rate has competing 3-D factors that can increase or decrease histogram overlap, the misclassification rates for the fractal cloud cases (bumpy top case and the flat top case) have a local minimum at a solar zenith angle of 37°($\mu_0 = 0.8$) in our simulations. For the fractal field with bumpy top case, the misclassification rate reaches its peak of 15% when the solar zenith angle is

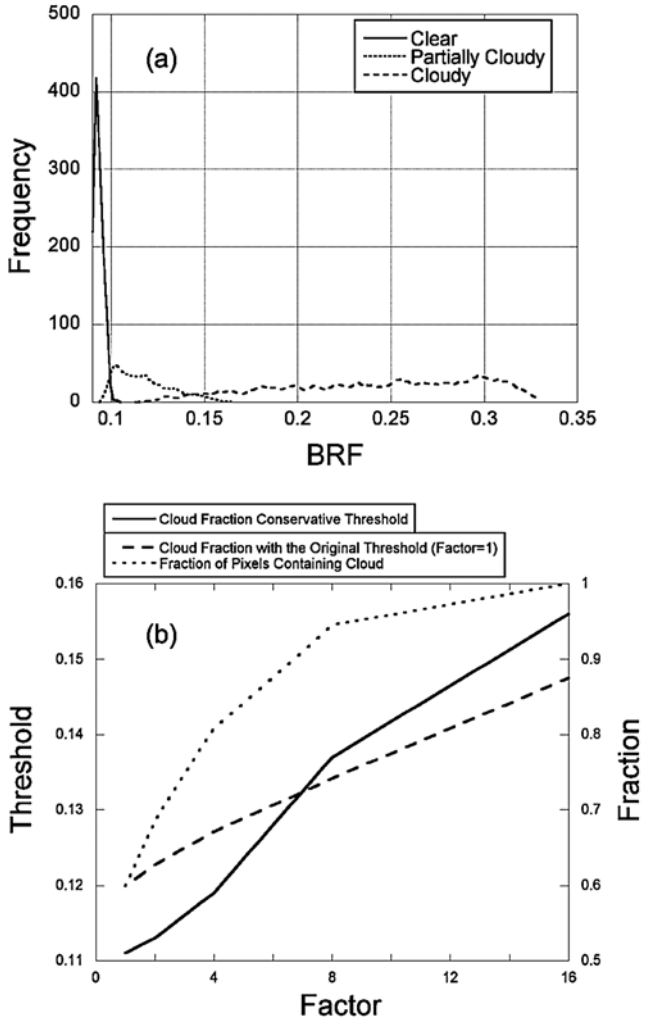

Figure 7. Resolution effect on histogram shape, threshold, and cloud fraction. Results are for the fractal case with bumpy top under overhead sun. Molecular scattering is included, aerosol optical depth is 0.1, and the surface is Lambertian with a reflectance of 5%. The full resolution histogram is shown in Figure 6d. (a) BRF histogram when resolution is degraded by a factor of 2. (b) Resolution dependence of threshold, cloud fraction and fraction of pixels containing partial cloud.

66°(μ_0 = 0.4). It decreases as the solar zenith angle increases over 66° (true for the flat top case too), which is due to the fact that almost all clear pixels are shadowed (ref. Figure 8) and the lowered BRF values make the clear pixels more distinguishable from the cloudy pixels.

[31] For the fractal cloud field, the misclassification rate is larger when cloud top is bumpy, indicating that the effects of the shadowing pathway may be dominating. However, for the LES cumulus cloud field, the misclassification rate for the bumpy top case is not everywhere larger than the flat top case, even though the misclassification rate of the flat top case does show smaller dependence on solar zenith angle. These results indicate that it may be difficult to rank the importance of the four 3-D pathways (Figure 2) that affect cloud detection.

[32] Figure 12 shows the domain averaged and maximum optical depths of the misclassified cloudy pixels as a function of solar zenith angle for the fractal (Figure 12a) and LES (Figure 12b) fields. As discussed in section 1, the misclassification of cloudy pixels arises from the darkened ones caused by the shadowing and leakage pathways. Figure 12 demonstrates that the bumpy top cases generally have a larger misclassified cloud optical depth for both fields. The domain averaged misclassification rates have a maximum value around 0.6 for both bumpy top cases. For the flat top cases, the values are slightly lower. However, the maximum cloud optical depth for misclassified cloudy pixels are much higher. For the fractal field (Figure 12a), the largest value is 2.8 for the bumpy top case and 1.2 for the flat top case. For the LES cumulus field (Figure 12b, the largest value is 4.9 for the bumpy top case and 3.0 for the flat top case. The misclassification of cloud pixels with optical depth of 4.9 is observed at a solar zenith angle of 66° (μ_0 = 0.4).

[33] An important climate variable that is often directly calculated from the cloud mask is the cloud fraction, calculated as the fraction of cloudy pixels identified by the cloud mask. Tremendous amount of efforts have been made to understand the quality of this product [e.g., *Shenk and Salomonson*, 1972; *Wielicki and Parker*, 1992; *Rossow et al.*, 1993; *Weare and Mokhov*, 1995; *Di Girolamo and Davies*, 1997; *Stowe et al.*, 1999; *Astin et al.*, 2001; *Zhao and Di Girolamo*, 2006]. As discussed in section 1, an unbiased cloud fraction can only be achieved by applying the cloud fraction conservative threshold. By assuming the clear mode of the histogram being symmetric about the clear sky value, *Wielicki and Parker* [1992] proposed a method to locate this threshold. However, the assumption made about the clear mode may not be universally valid, as shown in Figure 8 where the clear pixel distribution itself can be bimodal and asymmetric. To further complicate the matter, some observational studies [e.g., *Yang et al.*, 2007] show that the total histogram can be unimodal and the clear mode indistinguishable.

[34] To demonstrate how different thresholds affect the derived cloud faction, Figure 13 shows cloud fraction as a function of threshold type and solar zenith angle for the four simulated cloud scenes. It is expected that the cloud conservative threshold underestimates cloud fraction for all sun angles, while the clear conservative threshold overestimates it. In these simulations, the MCE threshold generally underestimates the cloud fraction, but tends to be close to the cloud fraction conservative threshold. The tendency of underestimation of the MCE threshold has been reported by *Yang et al.* [2007], where 16 automated thresholding algorithms, which are pursuing the MCE threshold, are applied to different derived quantities from observations, including BRF. Physically this is because more cloudy pixels are misclassified than clear pixels by the MCE threshold. As we can see from Figure 1 and Figure 8, there are generally more overlapped cloudy pixels than clear ones due to the fact that the standard deviation of the clear pixel distribution is smaller than the cloud pixel distribution. Also noticeable from Figure 13 is that the cloud fraction bias from different thresholds is at a

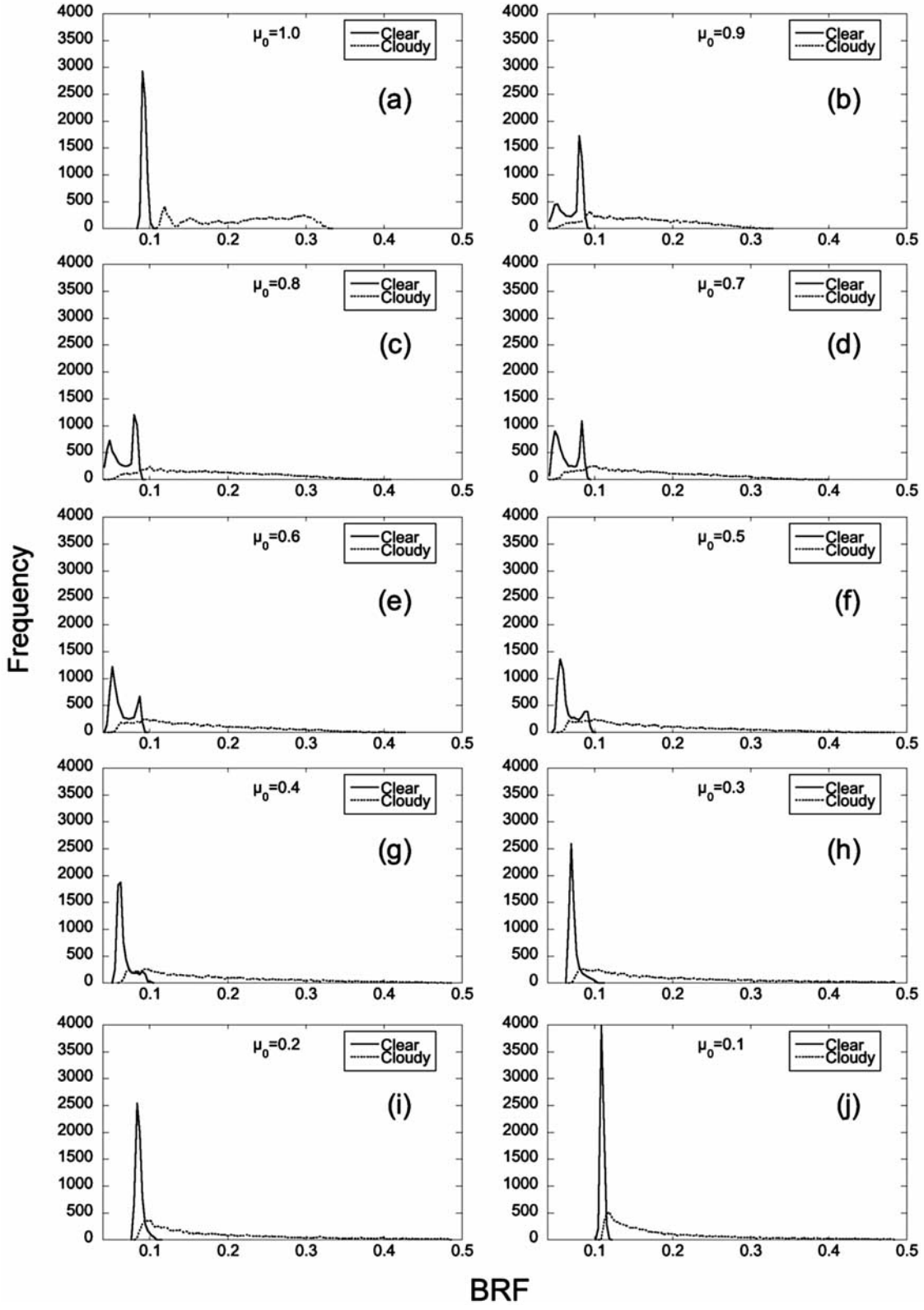

Figure 8. BRF histograms as they depend on the cosine of solar zenith angle (μ_0). Results are for the fractal cloud field with bumpy top with full resolution. Molecular scattering is included, aerosol optical depth is 0.1, and the surface is Lambertian with a reflectance of 5%. The histogram bin width is 0.004.

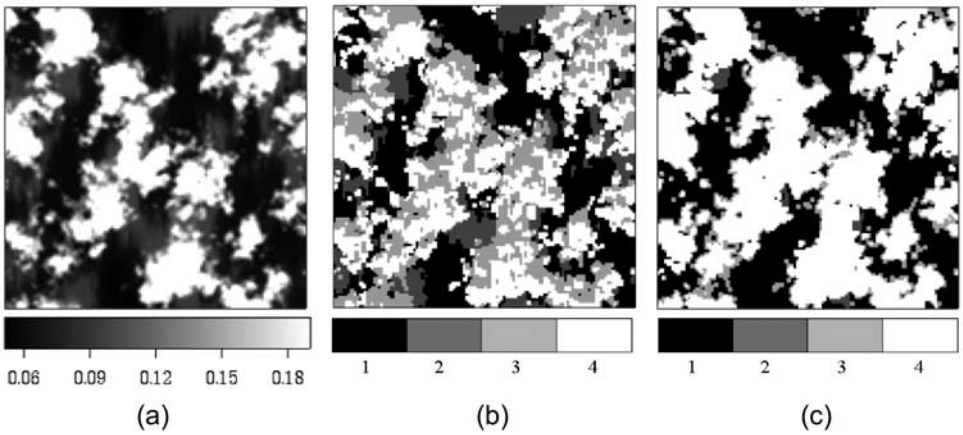

Figure 9. Location of the overlapped pixels. Results for the fractal cloud field with bumpy top. Molecular scattering is included, aerosol optical depth is 0.1, the surface is Lambertian with a reflectance of 5%, and $\mu_0 = 0.5$. (a) Simulated BRF image; (b) Shadow mask: 1, shadowed clear pixels; 2, not shadowed clear pixels; 3, shadowed cloudy pixels; 4, not shadowed cloudy pixels. (c) Overlapped and non-overlapped pixels: 1, Non-overlapped clear pixels; 2, overlapped clear pixels; 3, overlapped cloudy pixels; 4, non-overlapped cloudy pixels.

minimum for overhead Sun, which is consistent with the results drawn from Figure 11.

5. Consequences on Aerosol Optical Depth (AOD) Retrieval

[35] As discussed in section 1, cloud detection is an important step in deriving many geophysical products from satellites. Cloud detection errors caused by 3-D radiative effects will be carried over to these products. The impacts of different cloud masks on cloud fraction derivation have been discussed in section 4. Cloud masking biases caused by 3-D radiative effects could also have substantial impact on land surface remote sensing, sea surface temperature retrieval and other products. In this section, we analyze the

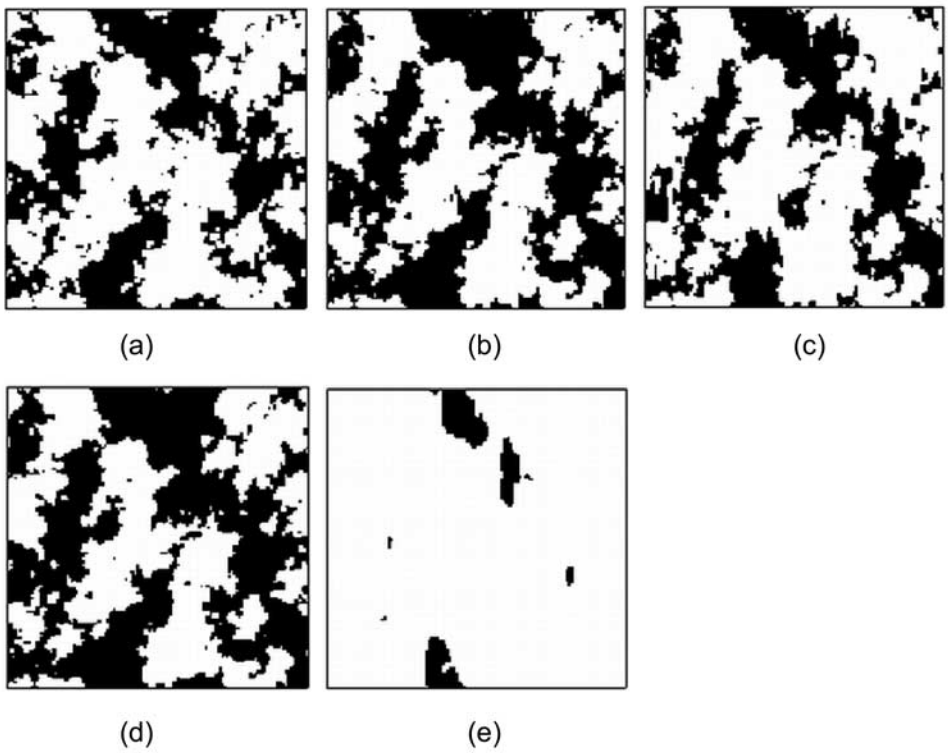

Figure 10. Different cloud masks for the BRF image shown in Figure 9a. (a) Perfect cloud mask, (b) cloud mask from the MCE threshold, (c) cloud mask from the cloud fraction conservative threshold, (d) cloud mask from the cloud conservative threshold, and (e) cloud mask from the clear conservative threshold. Black regions are classified as clear and white regions are classified as cloudy.

Table 1. Cloud Fraction Derived From Different Cloud Masks for the BRF Image Shown in Figure 9a and the Percentage of the Misclassification That Comes From Misclassified Clear/Cloudy Pixels

Cloud Mask	Cloud Fraction, %	Percentage of the Misclassification From Clear Pixels Misclassified as Cloudy, %	Percentage of the Misclassification From Cloudy Pixels Misclassified as Clear, %
Perfect	60	0	0
MCE	49	9	91
CF Conservative	60	50	50
Clear Conservative	89	100	0
Cloud Conservative	42	0	100

cloud masking consequences on the retrieval of aerosol optical depth.

5.1. Retrieval Process

[36] In this study, we adopt a single channel AOD retrieval procedure [e.g., *Stowe et al.*, 1997; *Ignatov and Stowe*, 2002]. Lookup tables are constructed to give the relationship between BRF values and aerosol optical depths for $0 \leq \mu_0 \leq 1$ at a μ_0 interval of 0.1 and an AOD interval of 0.01. Since the fractal cloud field and the LES cumulus field are layered differently, lookup tables are constructed for each field with the 1-D setup of the SHDOM model. The aerosol type and vertical scale factor are as described in section 2. In the retrieval of aerosol optical depth, the BRF from pixels labeled as clear by a cloud mask from the full 3-D simulations for a given μ_0 is mapped to AOD by searching through the lookup table. Retrievals are only done when $\mu_0 \geq 0.3$ because when the Sun is low, a small perturbation in BRF value, which might come from the limitation of modeling accuracy, would lead to a large difference in the retrieved aerosol optical depth.

[37] We examine the aerosol retrieval bias due to a combined 3-D radiative transfer and different cloud detection thresholds on a pixel basis and on a domain-averaged basis, which is reasonable since the true AOD is homogeneous across the model domain. The domain-averaged aerosol optical depths are retrieved in two different ways: (1) AOD is derived first for each individual pixel that is labeled clear by the cloud mask. Then the domain-averaged AOD is calculated by averaging all the successfully retrieved AOD; (2) the domain averaged BRF of all the pixels labeled clear by the cloud mask is calculated first. The AOD retrieval is done by using the domain averaged BRF value. The result from the first method is discussed in sections 5.2 and 5.3. Section 5.4 shows the result of the second method.

5.2. Biases of Pixel Based Aerosol Optical Depth Retrieval

[38] Figure 14 shows BRF enhancement images for clear pixels obtained from the perfect cloud mask due to 3-D radiative effects for overhead Sun (Figure 14a) and for $\mu_0 = 0.5$ (Figure 14c). The enhancement is defined as the difference between the BRF value obtained from 3-D simulations and from 1-D simulations, BRF_{3D}-BRF_{1D}. For overhead Sun (Figure 14a), all clear pixels are brightened by 3-D effects because of the channeling and surface-cloud interaction pathways and the absence of cloud shadows cast onto clear pixels. When $\mu_0 = 0.5$ (Figure 14c), cloud shadowing effect can darken some clear regions. With the lookup tables used in this study, if retrievals are done for these images, the brightened clear pixels will give positive biases and the darkened ones will give negative biases.

[39] Figures 14b and 14d show the retrieval biases of aerosol optical depth (AOD) for Figures 14a and 14c respectively. The biases are calculated as the retrieved minus the true AOD value, which is 0.1 in this case. As expected, for the overhead Sun (Figure 14b), the bias for every clear pixel is positive. For $\mu_0 = 0.5$ (Figure 14d), biases can be positive or negative depending on whether the pixel is shadowed or not. Note that retrievals are failed for a large portion of the clear pixels when $\mu_0 = 0.5$. The reason is that the BRF values for these pixels are too low - even lower than when aerosol optical depth equals 0 in the lookup table. We refer to these pixels as "overly darkened pixels" in our discussion.

[40] Figure 15 shows the dependence of domain averaged AOD retrieval biases, which are calculated by averaging all the successfully retrieved clear pixel AODs (i.e., not overly darkened), and the fraction of successfully retrieved clear pixels on solar zenith angle and cloud mask type for both the fractal field and the LES field with bumpy top case (the flat top cases have similar results to their bump top counterparts). The fraction of successfully retrieved clear pixels decreases with solar zenith angle due to the fact that lower Sun causes more shadows, and hence more overly darkened clear pixels. This is more prominent for the fractal field (Figure 15a) than the LES field because the former has higher cloud fraction,

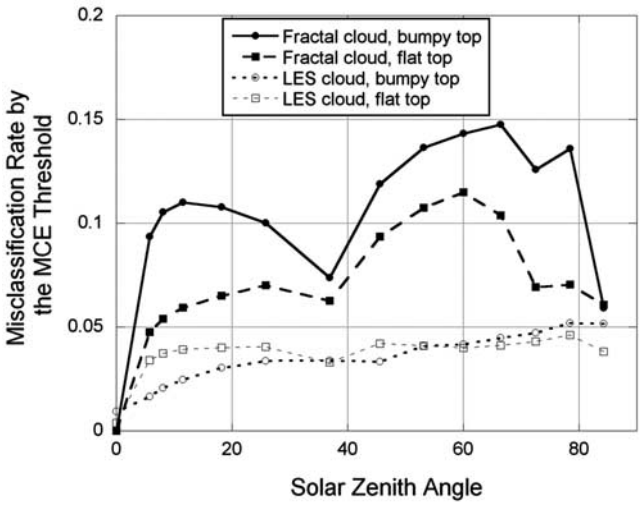

Figure 11. Misclassification rate of the MCE threshold as a function of solar zenith angle. Results are for simulations at full resolution. Molecular scattering is included, aerosol optical depth is 0.1, and the surface is Lambertian with a reflectance of 5%.

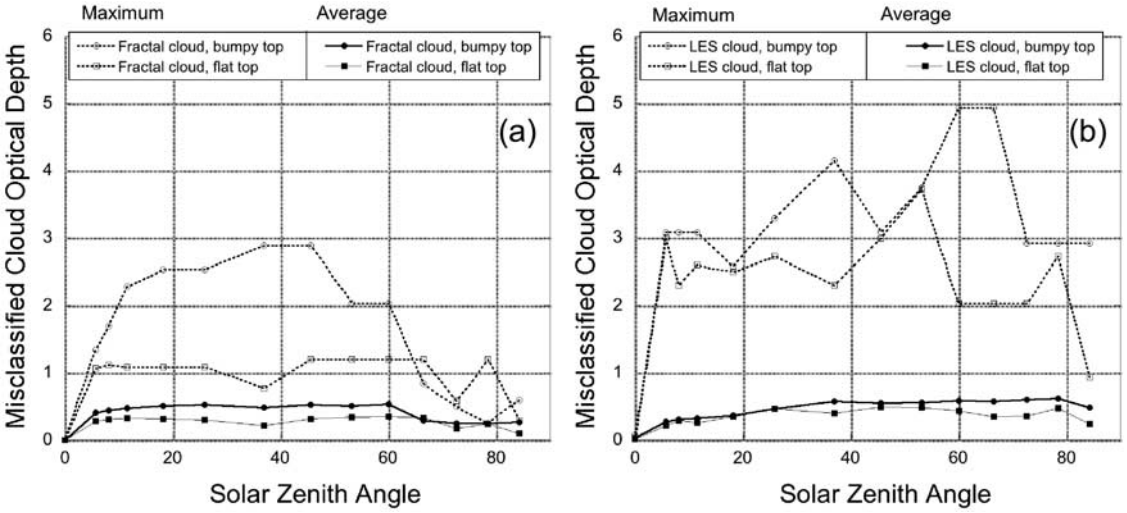

Figure 12. Domain averaged and maximum cloud optical depth for misclassified cloud pixels by the MCE threshold as a function of solar zenith angle. Results are for simulations at the full resolution. Molecular scattering is included, aerosol optical depth is 0.1, and the surface is Lambertian with a reflectance of 5%. (a) Results for the fractal field, and (b) results for the LES cumulus field.

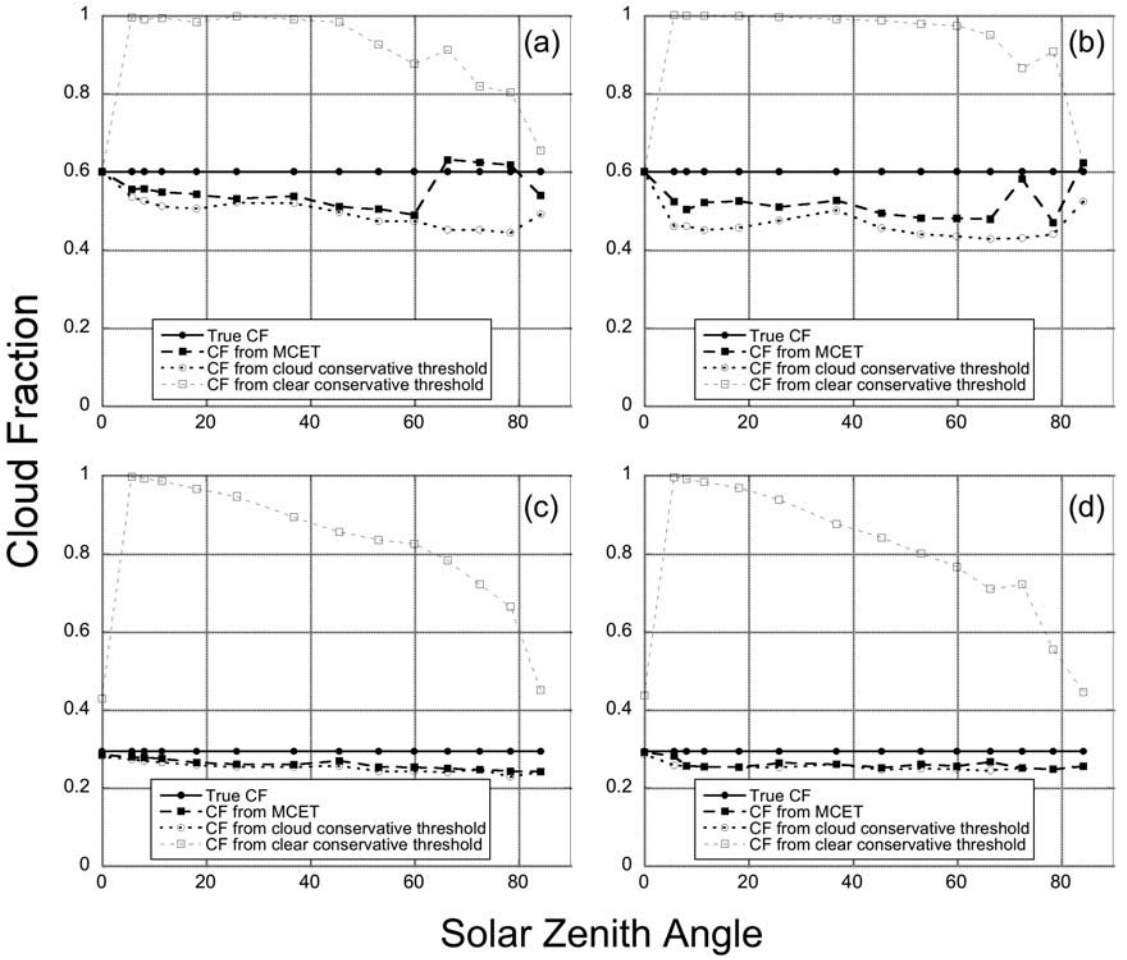

Figure 13. Cloud Fraction (CF) as a function of threshold and solar zenith angle. Results are for simulations at the full resolution. Molecular scattering is included, aerosol optical depth is 0.1, and the surface is Lambertian with a reflectance of 5%. (a) Fractal field with bumpy top, (b) fractal field with flat top, (c) LES cumulus field with bumpy top, and (d) LES cumulus field with flat top.

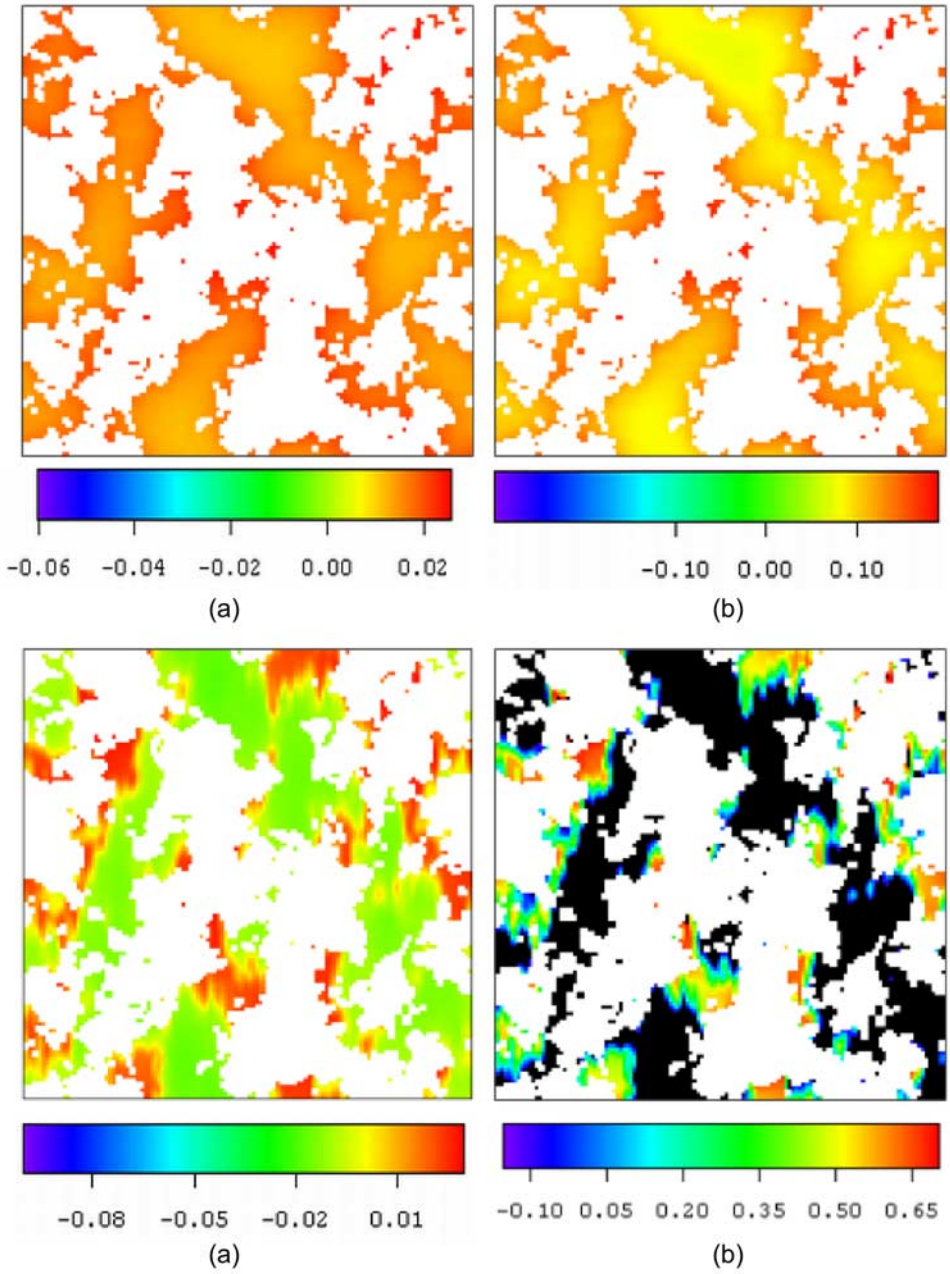

Figure 14. 3-D radiative effects over clear regions from the perfect cloud mask for the fractal case with bumpy top. True aerosol optical depth = 0.1. Molecular scattering is included, and the surface is Lambertian with a reflectance of 5%. (a) BRF enhancement for overhead Sun. White represents cloudy regions. (b) AOD retrieval bias for overhead Sun. White represents cloudy regions and black represents clear pixels that can not be retrieved. (c) Same as Figure 14a, except for $\mu_0 = 0.5$. (d) Same as Figure 14b, except for $\mu_0 = 0.5$.

hence larger portion of the clear pixels is covered by shadows when the Sun is not overhead. Clear pixels that have successful retrievals are mostly near the sun-facing cloud edges where they are not shadowed and this is the main reason why the retrievals are usually positively biased.

[41] Although one would expect that retrievals based on the clear conservative cloud mask would provide the least bias because of no cloud contamination, for the cases used in this study, the clear pixels identified by the clear conservative cloud masks are all overly darkened, except for overhead Sun as can be seen in Figure 8. Therefore Figure 15 does not include the clear-conservative cloud mask. For overhead Sun, misclassification of cloud detection is at a minimum, and the different cloud masks are either exactly the same (the fractal case) or very close to each other (the LES case), leading to similar AOD retrieval biases.

[42] Figure 15 demonstrates that retrievals based on three cloud masks, namely the perfect cloud mask, the cloud fraction conservative cloud mask and the MCE cloud mask, generally overestimate aerosol optical depth. For high Sun,

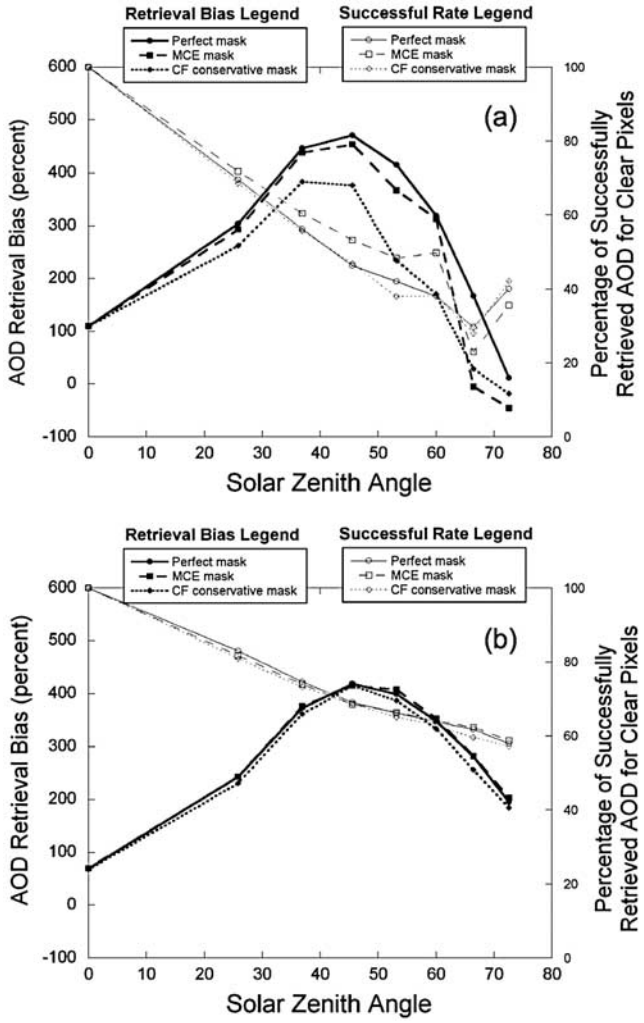

Figure 15. AOD retrieval bias and the fraction of successfully retrieved clear pixels as a function of cloud mask and solar zenith angle. True AOD = 0.1. Molecular scattering is included, and the surface is Lambertian with a reflectance of 5%. Results are for (a) the fractal field with bumpy top case, and (b) the LES cloud field with bumpy top case at full resolution.

the differences in the AOD bias from the different cloud masks are small because the cloud detection biases are small for all cloud masks (section 3.3). In this case, the fraction of successfully retrieved clear pixels is 100% and all clear pixels have brightened BRFs by the channeling and surface-cloud interaction pathways. This results in AOD biases ~100% for the fractal field (Figure 15a) and ~80% for the LES field (Figure 15b).

[43] The perfect and the MCE cloud masks give larger AOD biases than the cloud fraction conservative cloud mask. For all cases studied, the biases from the three cloud masks peak at a solar zenith angle in the range of 30° to 50°. Whether this is universally true needs to be further studied, but the fact that 3-D effect induced AOD retrieval bias is a function of solar zenith angle is confirmed. The retrieval biases can be very large. The maximum error reaches over 400% for the both cases shown in Figure 15.

[44] Another factor that affects the accuracy of aerosol optical depth retrieval is the spatial resolution of observation [e.g., *Henderson and Chylek*, 2005]. Figure 16 displays domain averaged retrieval biases as a function of resolution and solar zenith angle. Since all scenes show similar results, the results from the LES cloud field with bumpy top are used as an example. The domain averaged aerosol optical depth is calculated by averaging all the successfully retrieved AOD from clear pixels based on the perfect cloud mask. As shown in the figure, the retrieval bias decreases with decreasing spatial resolution in general, which is due to the fact that 3-D radiative effects become weaker away from clouds. The trend is similar for other cloud masks.

5.3. Aerosol Optical Depth Conservative Threshold

[45] As demonstrated above, 3-D radiative effects lead to biased aerosol optical depth retrievals, no matter whether the retrieval is based on the perfect cloud mask, cloud fraction conservative cloud mask or the MCE cloud mask. However, a threshold that conserves domain averaged aerosol optical depth can be defined. Figure 17 shows the AOD conservative threshold as well as clear conservative, cloud fraction conservative, cloud conservative and the MCE threshold for the image of Figure 9a. Note that for the AOD conservative threshold, some cloudy pixels are still misclassified as clear, to which AOD retrievals are applied. The AOD conservative threshold also lies between the clear-conservative threshold and the cloud fraction conservative threshold for this case.

[46] The cloud mask derived from the AOD conservative threshold shown in Figure 17 is displayed as Figure 18a. The cloud amount given by the AOD conservative cloud mask is higher than the perfect cloud mask, the cloud fraction conservative cloud mask, the MCE cloud mask and the cloud conservative cloud mask, but lower than the clear conservative cloud mask. However, not all of the pixels labeled clear have successfully retrieved AOD due

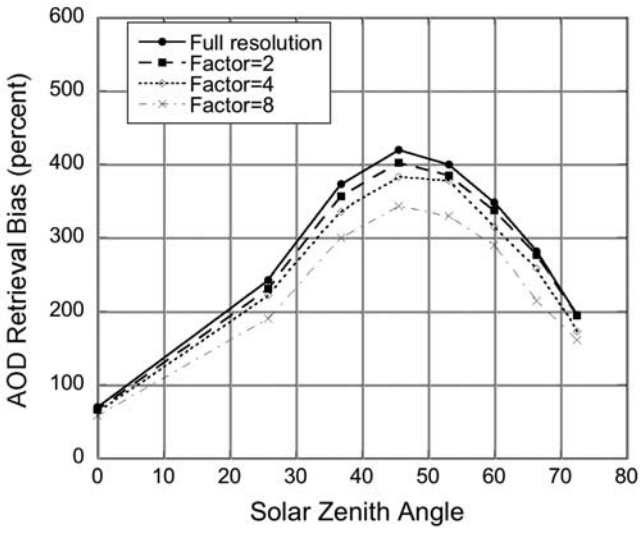

Figure 16. AOD retrieval bias as a function of resolution and solar zenith angle. Retrievals are based on the perfect cloud mask. True AOD = 0.1. Molecular scattering is included, and the surface is Lambertian with a reflectance of 5%. Results are for the LES cloud field with bumpy top case.

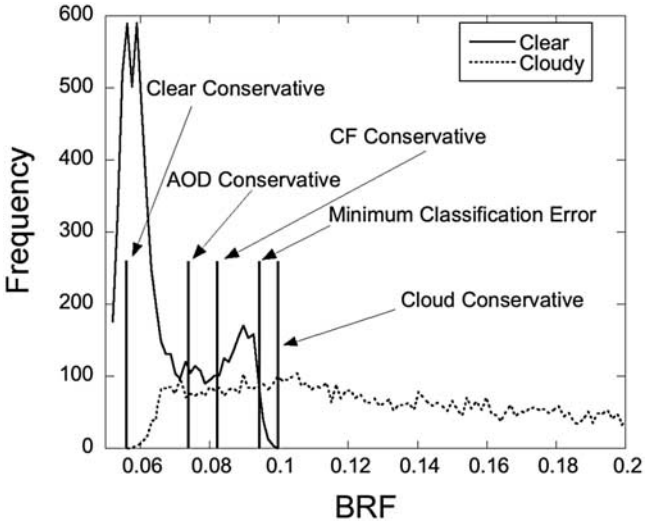

Figure 17. Histogram and thresholds for the image of Figure 9a. The two histograms are for clear pixels and cloudy pixels.

to the overly darkened pixels. Figure 18b shows the location of successfully retrieved AOD pixels; note the small portion of these pixels. This result is not only true for $\mu_0 = 0.5$, it is also true for most other sun angles. Figure 19 demonstrates this fact.

[47] On Figure 19, an AOD conservative threshold does not exist for overhead Sun because all the clear points in the field are brightened by 3-D radiative effects. In this case, no matter where the threshold is put, the retrieved AOD is positively biased. The AOD conservative cloud mask overestimates cloud fraction in general. The overestimation is larger for high Sun and decreases as the solar zenith angle increases. The reason is that for oblique Sun, more clear pixels are shadowed and the threshold shifts to the right side of the histogram in order to obtain the correct domain averaged AOD.

5.4. AOD Retrievals Based on Domain Averaged BRF

[48] A second approach to retrieving domain averaged AOD is to calculate the domain averaged clear pixel BRF first and then do the retrieval [e.g., *Stowe et al.*, 1997]. Figure 20 shows the AOD retrieved in this way as a function of solar zenith angle for several cloud masks for the fractal field and the LES cloud field with bumpy top case. Retrievals are for simulations at full resolution. Compared to Figure 15, the biases in Figure 20 are much smaller, which is because some of the clear pixel BRFs are brightened by 3-D effects while others are darkened so that the average is closer to BRF from IPA radiative transfer simulations. For the fractal field (Figure 20a), there are no retrievals for the MCE mask and the cloud conservative mask at several points when the Sun is low. This is due to the overly darkening effect where the domain-averaged BRFs are too low. Depending on the scene, solar zenith angle and cloud mask type, the retrieval biases can be either positive or negative. An AOD conservative threshold can also be derived for retrievals with this method. When applied to the same example as Figure 17, the AOD conservative threshold for this method (not shown) is located at a position between the cloud fraction conservative threshold and the MCE threshold.

[49] Part of the MODIS AOD retrieval algorithm adopts another way to minimize the impact of 3-D radiative and cloud contamination effects [*Kaufman et al.*, 2005]. It uses the average of the 25th to 75th percentile (sorted by BRF) of the clear pixels for the retrieval of the 10×10 km^2 box in hopes of eliminating residual cloud contamination and cloud shadows (it should be noted that MODIS also uses a spatial homogeneity test with 3×3 500-m pixel arrays to screen clouds [*Martins et al.*, 2002]). Figure 21 shows the results from simulating the MODIS method. Even though smaller than what is shown in Figure 15, the biases of the retrievals from this method are still significant for the cases studied here. The maximum bias is ~200% for the fractal case (Figure 21a) and ~300% for the LES case. The large

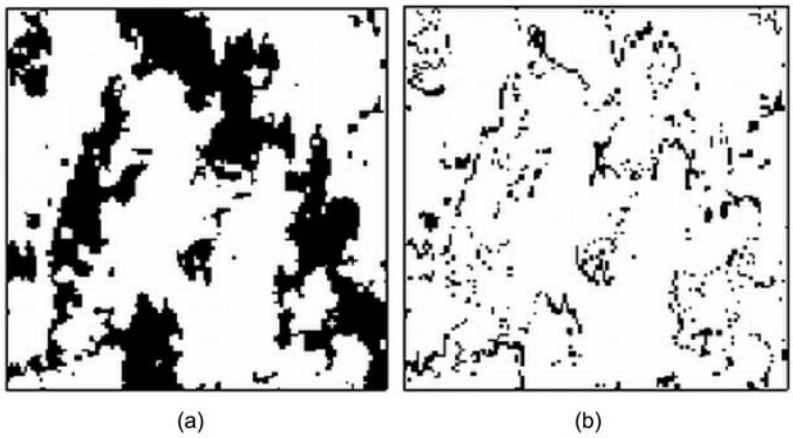

Figure 18. Cloud masks for the retrieval of unbiased AOD for the image shown in Figure 9a. (a) Aerosol optical depth conservative cloud mask - black regions are pixels labeled clear and white regions are pixels labeled cloudy; (b) A mask that shows pixels that have successfully retrieved AOD - black represents the pixels successfully retrieved and white represents pixels either labeled cloudy or clear pixels where retrievals have failed.

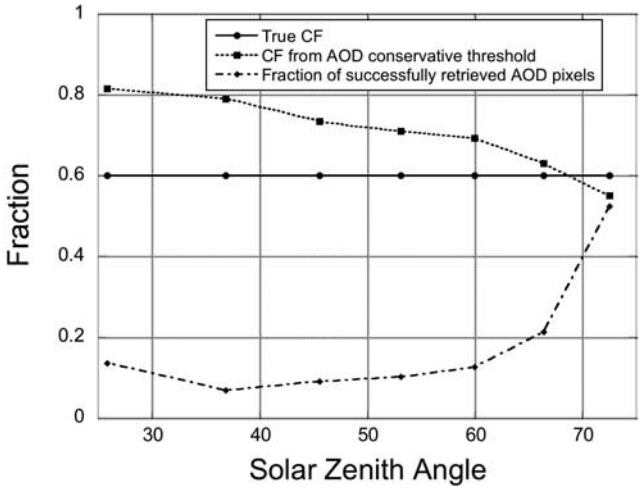

Figure 19. Cloud fraction and the fraction of successfully retrieved AOD pixels for the AOD conservative cloud mask as a function of solar zenith angle. Input AOD = 0.1. Molecular scattering is included, and the surface is Lambertian with a reflectance of 5%. Results are for fractal field with bumpy top.

difference between Figures 15, 20 and 21 demonstrates the importance of the sampling strategy for selecting BRF values within a domain for the purpose of retrieving AOD. For this method, the location of the AOD conservative threshold moves further right compared to the method above when applied to the same example as Figure 17. For this example, the AOD conservative threshold for this method (not shown) is located at a position between the MCE threshold and the clear fraction conservative threshold. The change of AOD conservative threshold values for different approaches suggests that the approach used in retrieving the domain averaged AOD and the cloud mask must be considered simultaneously when developing a domain averaged AOD product.

6. Summary and Discussion

[50] The purpose of this study is to understand how 3-D radiative effects contribute to cloud detection errors and how these errors are carried over to the retrieval of cloud fraction and aerosol optical depth for a variety of threshold types. Cloud detection is accomplished by thresholding the 0.67 μm BRF, which is one of the most popular cloud detection tests [e.g., *Saunders and Kriebel*, 1988; *Rossow and Garder*, 1993b; *Ackerman et al.*, 1998; *Baum and Trepte*, 1999; *Stowe et al.*, 1999], and by itself detects most of the clouds over ocean in the MODIS operational cloud mask product [*Ackerman et al.*, 2007]. By simulating the radiative transfer process through predefined heterogeneous cloud fields over a Lambertian surface at the wavelength of 0.67 μm at nadir with SHDOM and applying the standard procedures of cloud detection followed by cloud fraction and aerosol optical depth retrievals to the simulated images, this study shows the following results:

[51] (1) 3-D effects cause increases in histogram overlap between distributions of clear and cloudy pixels. Because of this fact, perfect satellite cloud detection is practically impossible through single thresholding techniques even when there is no background variability and no instrument noise.

[52] (2) A good cloud detection scheme must be purpose-oriented. Different cloud masks, such as, the clear conservative cloud mask, cloudy conservative cloud mask, cloud fraction conservative cloud mask and the cloud mask from the minimum classification error (MCE) threshold, can be defined for different applications. For the MCE threshold, clear pixels that have been misclassified as cloud tend to occur when they are not shadowed by the cloud, but are near

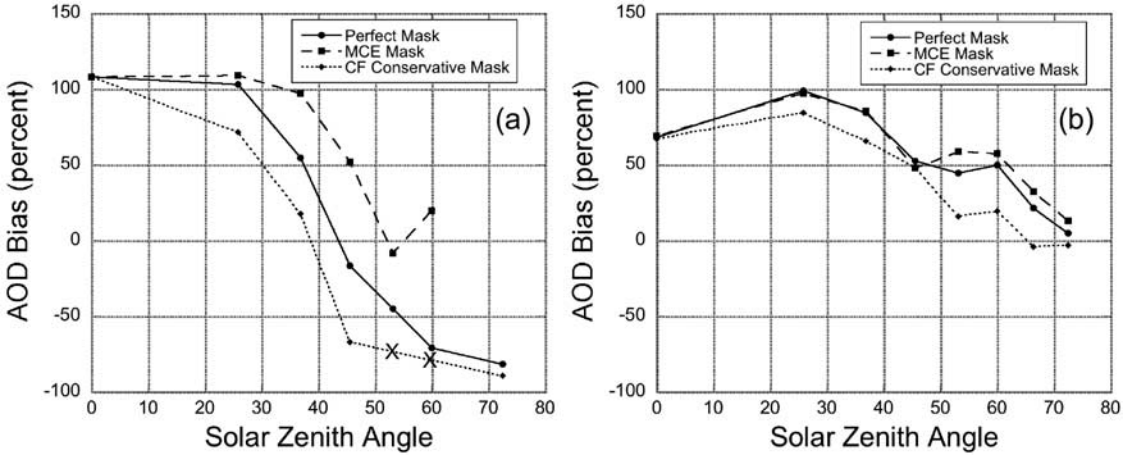

Figure 20. Biases of AODs retrieved from domain averaged BRFs of all clear pixels as a function of cloud mask and solar zenith angle. Results are for simulations at the full resolution. True AOD = 0.1. Molecular scattering is included, and the surface is Lambertian with a reflectance of 5%. Retrievals are for the following 8 solar positions: 0° ($\mu_0 = 1$); 25.8° ($\mu_0 = 0.9$); 36.9° ($\mu_0 = 0.8$); 45.6° ($\mu_0 = 0.7$); 53.1° ($\mu_0 = 0.6$); 60° ($\mu_0 = 0.5$); 66.4° ($\mu_0 = 0.4$); and 72.5° ($\mu_0 = 0.3$). The missing points (e.g., the result at 72.5° for the MCE mask and the points with a "X" sign are the ones that are not successfully retrieved due the overly darkened pixel problem. (a) Fractal field with bumpy top, and (b) LES cumulus field with bumpy top.

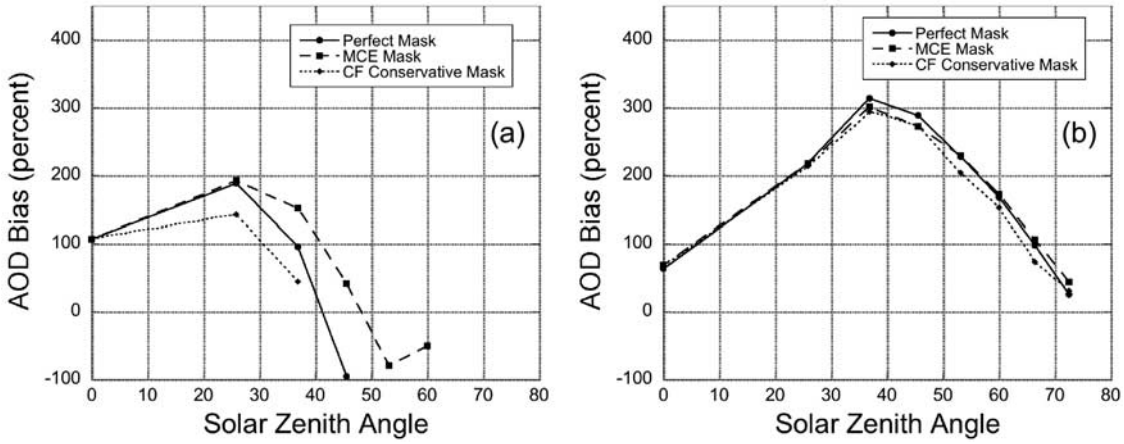

Figure 21. Same as Figure 20, except for biases of AOD retrievals from domain averaged BRFs of 25th to 75th percentile (sorted by BRF) of the clear pixels. (a) Fractal field with bumpy top, and (b) LES cumulus field with bumpy top.

cloud edges. Cloudy pixels that are misclassified as clear occur when they are shadowed by other clouds, or are pixels containing optically thin clouds.

[53] (3) Molecular and aerosol scattering, surface reflectance, 3-D distribution of cloud extinction coefficients, and resolution effects all contribute to the degree to which the clear and cloudy portions of the histogram overlap through channeling, leakage, shadowing and surface-cloud interaction pathways. Ranking the importance of each pathway to the degree of clear-cloud overlap was situation-dependent. However, for a given solar zenith angle, the pronounced impact of the surface-cloud interaction to brightening the clear BRF values, which contributes to the clear-cloud overlap, suggests that all quantitative results presented in this study will be sensitive to the treatment of surface reflectance.

[54] (4) The misclassification rate using the MCE threshold, which is the threshold that minimizes misclassification, is a function of solar zenith angle and is minimized when the Sun is overhead. The dependence of misclassification rates with solar zenith angle implies that the quality of cloud detection will have, for example, a latitudinal dependence and a dependence on the time of observation. This suggests that the quality of geophysical products that use a cloud mask will depend on solar zenith angle, thus limiting the conclusions drawn from spatial and temporal trend analyzes of satellite cloud and aerosol products.

[55] (5) When the Sun is oblique, clouds with fairly large optical depth can be misclassified as clear by the MCE threshold. Misclassification of cloud pixels with optical depth of 4.9 has been observed in one simulation having a solar zenith angle around 60°.

[56] (6) Different thresholds give different cloud fraction biases. Only the cloud fraction conservative threshold provides the right cloud amount. The cloud fraction derived from the MCE threshold is closest to the true value, but with a tendency to underestimate it. The cloud conservative threshold underestimates the cloud fraction and the clear conservative threshold highly overestimates it.

[57] (7) The consequence of cloud masking and 3-D radiative effects on aerosol optical depth retrieval is significant, reaching an overestimate of more than 400% in domain averaged AOD in the simulations. A perfect cloud mask does not necessarily result in a better AOD retrieval. For the cases studied in this article, biases reach their peak at a solar zenith angle in the range of 30° to 50°.

[58] (8) As the resolution decreases, the pixel-level AOD retrieval bias decreases because clear pixels contain areas that are further away from clouds where 3-D radiative effects become weaker.

[59] (9) An aerosol optical depth conservative cloud mask can be derived. The value of the AOD conservative threshold depends on the sampling approaches. This suggests that the approach used in retrieving the domain averaged AOD and the cloud mask must be considered simultaneously when developing a domain averaged AOD product.

[60] (10) Compared to results from averaging AODs of all successfully retrieved pixels, retrieval biases are significantly smaller when obtained from domain averaged BRFs of all clear pixels or from domain averaged BRFs of 25th to 75th percentile (sorted by BRF) of the clear pixels. The reason is that the clear pixels brightened by 3-D radiative effects and those darkened by 3-D radiative effects cancel each other to some degree. These three sampling approaches for computing domain-averaged AOD produced very different AOD values, even when they are all using the same cloud mask, highlighting the importance in the sampling strategy used in reporting domain-averaged AOD values.

[61] It should be pointed out that the results obtained in this study are for rather small spatial domains, very fine resolutions, only for several scenes, and do not include other sources of errors, such as assumptions of aerosol and surface scattering and absorption properties and the potential for the misidentification of thin cirrus clouds. In no way are the errors reported here for cloud detection, cloud fraction and AOD-retrievals representative of the overall quality of any real operational product. Rather, we sought physical insight on the connection between these retrievals caused by 3-D radiative effects. However, the possibility of large AOD retrieval biases caused by 3-D radiative effects has been confirmed by a recent study by *Wen et al.* [2007], which observed a 140% AOD retrieval bias in the MODIS aerosol product for a particular time and place surrounded by

cumulus clouds. Our results do suggest that the large differences observed in various climatologies derived from different satellites [e.g., *Myhre et al.*, 2004] may be in part due to the different orbital configuration of the satellites, which determines the solar zenith angles that are sampled, and the different sampling strategies employed in deriving the domain-averaged AOD that is reported in the satellite data sets.

[62] **Acknowledgments.** The authors would like to thank Dr. Frank Evans for providing the SHDOM model and Dr. Tamás Várnai for providing the fractal cloud model used in this study. Partial support from the Jet Propulsion Laboratory, California Institute of Technology, under a contract with the National Aeronautics and Space Administration is gratefully acknowledged.

References

Acharya, P. K., et al. (1998), MODTRAN User's Manual Versions 3.7 and 4.0, Air Force Research Laboratory.

Ackerman, S. A., K. I. Strabala, W. P. Menzel, R. A. Frey, C. C. Moeller, and L. E. Gumley (1998), Discriminating clear sky from clouds with MODIS, *J. Geophys. Res.*, *103*(D24), 32,141–32,157.

Ackerman, S. A., R. Holtz, R. A. Frey, E. Eloranta, B. Maddux, and M. McGill (2007), Cloud detection with MODIS: Part II Validation, *J. Atmos. Oceanic Technol.*, in press.

Astin, I., L. Di Girolamo, and H. M. Van De Poll (2001), Bayesian confidence intervals for true fractional coverage from finite transect measurements: Implications for cloud studies from space, *J. Geophys. Res.*, *106*(D15), 17,303–17,310.

Baum, B. A., and Q. Trepte (1999), A grouped threshold approach for scene identification in AVHRR imagery, *J. Atmos. Oceanic Technol.*, *16*(6), 793–800.

Berendes, T. A., D. A. Berendes, R. M. Welch, E. G. Dutton, T. Uttal, and E. E. Clothiaux (2004), Cloud cover comparisons of the MODIS daytime cloud mask with surface instruments at the North Slope of Alaska ARM site, *IEEE Trans. Geosci. Remote Sens.*, *42*(11), 2584–2593.

Cahalan, R. F., et al. (2005), The 13RC - Bringing together the most advanced radiative transfer tools for cloudy atmospheres, *Bull. Am. Meteorol. Soc.*, *86*(9), 1275–1293.

Cahalan, R. F., L. Oreopoulos, G. Wen, A. Marshak, S. C. Tsay, and T. DeFelice (2001), Cloud characterization and clear-sky correction from Landsat-7, *Remote Sens. Environ.*, *78*(1–2), 83–98.

Di Girolamo, L., and R. Davies (1997), Cloud fraction errors caused by finite resolution measurements, *J. Geophys. Res.*, *102*(D2), 1739–1756.

Di Girolamo, L., T. Várnai, and R. Davies (1998), Apparent breakdown of reciprocity in reflected solar radiances, *J. Geophys. Res.*, *103*(D8), 8795–8803.

Evans, K. F. (1998), The spherical harmonics discrete ordinate method for three-dimensional atmospheric radiative transfer, *J. Atmos. Sci.*, *55*(3), 429–446.

Glasbey, C. A. (1993), An analysis of histogram-based thresholding algorithms, *CVGIP: Graphical Models and Image Processing*, *55*(6), 532–537.

Henderson, B. G., and P. Chylek (2005), The effect of spatial resolution on satellite aerosol optical depth retrieval, *IEEE Trans. Geosci. Remote Sens.*, *43*(9), 1984–1990.

Ignatov, A., and L. Stowe (2002), Aerosol retrievals from individual AVHRR channels. Part I: Retrieval algorithm and transition from Dave to 6S radiative transfer model, *J. Atmos. Sci.*, *59*(3), 313–334.

Kaufman, Y. J., et al. (2005), A critical examination of the residual cloud contamination and diurnal sampling effects on MODIS estimates of aerosol over ocean, *IEEE Trans. Geosci. Remote Sens.*, *43*(12), 2886–2897.

Kittler, J., and J. Illingworth (1986), Minimum error thresholding, *Pattern Recognition*, *19*(1), 41–47.

Koren, I., and J. H. Joseph (2000), The histogram of the brightness distribution of clouds in high-resolution remotely sensed images, *J. Geophys. Res.*, *105*(D24), 29,369–29,377.

Loeb, N. G., and J. A. Coakley (1998), Inference of marine stratus cloud optical depths from satellite measurements: Does 1D theory apply?, *J. Clim.*, *11*(2), 215–233.

Loeb, N. G., and R. Davies (1997), Angular dependence of observed reflectances: A comparison with plane parallel theory, *J. Geophys. Res.*, *102*(D6), 6865–6881.

Marshak, A., A. Davis, W. Wiscombe, and R. Cahalan (1995), Radiative smoothing in fractal clouds, *J. Geophys. Res.*, *100*(D12), 26,247–26,261.

Marshak, A., S. Platnick, T. Várnai, G. Y. Wen, and R. F. Cahalan (2006), Impact of three-dimensional radiative effects on satellite retrievals of cloud droplet sizes, *J. Geophys. Res.*, *111*(D9), D09207, doi:10.1029/2005JD006686.

Martins, J. V., D. Tanré, L. Remer, Y. Kaufman, S. Mattoo, and R. Levy (2002), MODIS Cloud screening for remote sensing of aerosols over oceans using spatial variability, *Geophys. Res. Lett.*, *29*(12), 8009, doi:10.1029/2001GL013252.

Myhre, G., et al. (2004), Intercomparison of satellite retrieved aerosol optical depth over the ocean, *J. Atmos. Sci.*, *61*(5), 499–513.

Nikolaeva, O. V., L. P. Bass, T. A. Germogenova, A. A. Kokhanovsky, V. S. Kuznetsov, and B. Mayer (2005), The influence of neighbouring clouds on the clear sky reflectance studied with the 3-D transport code RADUGA, *J. Quant. Spectrosc. Radiat. Transfer*, *94*(3–4), 405–424.

Pal, N. R., and D. Bhandari (1993), Image thresholding - Some new techniques, *Signal Processing*, *33*(2), 139–158.

Prewitt, J. M. S., and M. L. Mendelsohn (1966), The analysis of cell images, *Ann. N.Y. Acad. Sci.*, *128*, 1035–1053.

Rossow, W. B. (1989), Measuring cloud properties from space: A review, *J. Clim.*, *2*(3), 201–213.

Rossow, W. B., and L. C. Garder (1993a), Validation of ISCCP cloud detections, *J. Clim.*, *6*(12), 2370–2393.

Rossow, W. B., and L. C. Garder (1993b), Cloud detection using satellite measurements of infrared and visible radiances for ISCCP, *J. Clim.*, *6*(12), 2341–2369.

Rossow, W. B., et al. (1985), ISCCP Cloud algorithm intercomparison, *J. Appl. Meteorol.*, *24*(9), 877–903.

Rossow, W. B., A. W. Walker, and L. C. Garder (1993), Comparison of ISCCP and other cloud amounts, *J. Clim.*, *6*(12), 2394–2418.

Saunders, R. W., and K. T. Kriebel (1988), An improved method for detecting clear sky and cloudy radiances from AVHRR data, *Int. J. Remote Sens.*, *9*(1), 123–150.

Shenk, W. E., and V. V. Salomonson (1972), A simulation study exploring the effects of sensor spatial resolution on estimates of cloud cover from satellites, *J. Appl. Meteorol.*, *11*(1), 214–220.

Stowe, L. L., A. M. Ignatov, and R. R. Singh (1997), Development, validation, and potential enhancements to the second-generation operational aerosol product at the national environmental satellite, data, and information service of the national oceanic and atmospheric administration, *J. Geophys. Res.*, *102*(D14), 16,923–16,934.

Stowe, L. L., P. A. Davis, and E. P. McClain (1999), Scientific basis and initial evaluation of the CLAVR-1 global clear/cloud classification algorithm for the advanced very high resolution radiometer, *J. Atmos. Oceanic Technol.*, *16*(6), 656–681.

Strahler, A. H. (1980), The use of prior probabilities in maximum-likelihood classification of remotely sensed data, *Remote Sens. Environ.*, *10*(2), 135–163.

Thomas, S. M., A. K. Heidinger, and M. J. Pavolonis (2004), Comparison of NOAA's operational AVHRR-derived cloud amount to other satellite-derived cloud climatologies, *J. Clim.*, *17*(24), 4805–4822.

Várnai, T. (1996), *Reflection of solar radiation by inhomogeneous clouds*, McGill University, 149 pp.

Várnai, T., and A. Marshak (2001), Statistical analysis of the uncertainties in cloud optical depth retrievals caused by three-dimensional radiative effects, *J. Atmos. Sci.*, *58*(12), 1540–1548.

Várnai, T., and A. Marshak (2003), A method for analyzing how various parts of clouds influence each other's brightness, *J. Geophys. Res.*, *108*(D22), 4706, doi:10.1029/2003JD003561.

Weare, B. C. (1995), Factors controlling ERBE longwave clear sky and cloud forcing fluxes, *J. Clim.*, *8*(7), 1889–1899.

Weare, B. C., and I. I. Mokhov (1995), Evaluation of total cloudiness and its variability in the atmospheric model intercomparison project, *J. Clim.*, *8*(9), 2224–2238.

Wen, G. Y., R. F. Cahalan, S. C. Tsay, and L. Oreopoulos (2001), Impact of cumulus cloud spacing on Landsat atmospheric correction and aerosol retrieval, *J. Geophys. Res.*, *106*(D11), 12,129–12,138.

Wen, G. Y., A. Marshak, and R. F. Cahalan (2006), Impact of 3-D clouds on clear-sky reflectance and aerosol retrieval in a biomass burning region of Brazil, *IEEE Trans. Geosci. Remote Sens. Lett.*, *3*(1), 169–172.

Wen, G. Y., A. Marshak, R. F. Cahalan, L. A. Remer, and R. G. Kleidman (2007), 3D Aerosol-cloud radiative interaction observed in collocated MODIS and ASTER images of cumulus cloud fields, *J. Geophys. Res.*, *112*, D13204, doi:10.1029/2006JD008267.

Wielicki, B. A., and L. Parker (1992), On the determination of cloud cover from satellite sensors - The effect of sensor spatial-resolution, *J. Geophys. Res.*, *97*(D12), 12,799–12,823.

Wielicki, B. A., and R. M. Welch (1986), Cumulus cloud properties derived using Landsat satellite data, *J. Clim. Appl. Meteorol.*, *25*(3), 261–276.

Yang, Y., L. Di Girolamo, and D. Mazzoni (2007), Selection of the automated thresholding algorithm for the multi-angle imaging spectro radiometer radiometric camera-by-camera cloud mask over land, *Remote Sens. Environ.*, *107*, 159–171.

Zhao, G., and L. Di Girolamo (2006), Cloud fraction errors for trade wind cumuli from EOS-Terra instruments, *Geophys. Res. Lett.*, *33*, L20802, doi:10.1029/2006GL027088.

L. Di Girolamo, Department of Atmospheric Sciences, University of Illinois at Urbana-Champaign, Urbana, IL, USA.

Y. Yang, Goddard Earth Science and Technology Center, University of Maryland at Baltimore County, Baltimore, MD 21228, USA. (yuekui@umbc.edu)